

Electronic Supplementary Information (ESI)

Wide-temperature-range operation of lithium-metal batteries using partially and weakly solvating liquid electrolytes

Saehun Kim,^{‡a} Jeong-A Lee,^{‡a} Tae Kyung Lee,^{‡b} Kyungeun Baek,^c Juyoung Kim,^c Boguen Kim,^a Jeong Hwan Byun,^a Hyun-Wook Lee,^c Seok Ju Kang,^c Ji-Ae Choi,^d So-Young Lee,^d Moon-Hyung Choi,^d Jong-Hyun Lee^d and Nam-Soon Choi^{*a}

^aDepartment of Chemical and Biomolecular Engineering, Korea Advanced Institute of Science and Technology (KAIST), 291 Daehak-ro, Yuseong-gu, Daejeon, 34141, Republic of Korea.

^bDepartment of Materials Engineering and Convergence Technology, Gyeongsang National University (GNU), Jinju 52828, Republic of Korea.

^cDepartment of Energy Engineering, School of Energy and Chemical Engineering, Ulsan National Institute of Science and Technology (UNIST), 50 UNIST-gil, Ulsan 44919, Republic of Korea.

^dSolvay Specialty Polymers Korea, Solvay Research & Innovation Center, 150 Bugahyeon-ro, Seodaemun-gu, Seoul 03759, Republic of Korea.

*Correspondence to: nschoi@kaist.ac.kr

Supplementary Experimental Section

Electrochemical Evaluations

To compare the capacity retention of Li|LiCoO₂ full cells at low-temperature compared to that at room-temperature, fully charged full cells at room-temperature were discharged at 0 °C, -20 °C, and -30 °C, respectively. The fast-charging performance of the Li|LiCoO₂ full cell was evaluated by sequentially increasing the charging C-rate to C/3, C/2, 1C, 2C, 3C, 5C, 7C, and 10C at a fixed discharge rate of C/3. After the 10C evaluation, capacity retention was examined at a charging C-rate of C/3. The evaluation voltage range was set at 3.0–4.4 V vs. Li/Li⁺. The Li⁺ transference number of each electrolyte was calculated using the Bruce–Vincent method and monitored in Li|Li cells using a combination of DC polarization and electrochemical impedance spectroscopy (EIS). A constant polarization bias (ΔV) of 5 mV was applied to record the initial (I_0) and steady-state (I_{ss}) currents, along with the impedance before (R_0) and after (R_{ss}) polarization. For EIS, a constant voltage between 1 MHz and 10 mHz was applied under open-circuit conditions to record the impedance before (R_0) and after (R_{ss}) polarization. Subsequently, the Li⁺ transference number was calculated with the following equation.¹

$$\text{Li}^+ \text{ transference number: } \frac{I_{ss}(\Delta V - I_0 R_0)}{I_0(\Delta V - I_{ss} R_{ss})}$$

The aforementioned cells were all fabricated in an argon-filled glovebox.

Characterization

To monitor the chemical composition of 1,2-bis(1,1,2,2-tetrafluoroethoxy)ethane (TFEE), it was analyzed by 500-MHz ¹H, ¹³C, ¹⁷O, and ¹⁹F NMR spectroscopy using a coaxial nuclear magnetic resonance (NMR) tube (Willmad-LabGlass). THF-d₈ (99.5%, NMR grade, BK Instruments Inc.) with 1 wt.% of hexafluorobenzene (C₆F₆, 99.5%, NMR grade, Sigma-

Aldrich) was used as an internal standard for NMR analysis. Donor number (DN) of 1,2-dimethoxyethane (DME) and TFEE was measured by ^{23}Na analysis. 20 mM of NaTFSI was dissolved in DME and TFEE respectively, for DN measurement.² 0.5M NaClO₄ D₂O was used as an internal reference for ^{23}Na NMR analysis. DN was calculated by the following equation: $(2.106 \cdot \delta) + 32.74$. The amount of free solvents (DME and TFEE) in the electrolytes was analyzed by Fourier Transform Infrared Spectroscopy (FT-IR). For EIS, a constant voltage between 1 MHz and 10 mHz was applied under open-circuit conditions to record the resistance of the SEI during cycling (10th, 30th, and 50th cycles) with each electrolyte. In-situ DEMS analysis was used to monitor the gas evolution during the first charging of the Li|LiCoO₂ full cells with LiFSI DME (1.3 M) (LCE), LiFSI DME/TFEE (1.3 M; 2/8, v%) (PWSE), and LiFSI DME/TFEE (1.3 M; 2/8, v%)+1% LiFMDFB+0.05% AgNO₃ (PWSE+LiFMDFB+AgNO₃) from the open-circuit voltage (OCV) to 4.8 V vs. Li/Li⁺ under 25 °C. The gas evolution in the cells was detected at 5 min intervals. The amount of transition-metal deposition on the Li-metal anodes after a storage test at 60 °C for 10 days was analyzed using Time-of-Flight Secondary Ion Mass Spectrometry (TOF-SIMS). Thermogravimetric analysis (TGA) was used to analyze the volatility of DME, 1,1,2,2-tetrafluoroethyl-2,2,3,3-tetrafluoropropyl ether (TTE), TFEE, LHCE, and PWSE in the temperature range of 30 °C to 150 °C under a N₂ environment.

Supplementary Notes

Note S1. Peak shift of LiFSI in PWSE structure (^{17}O NMR)

The ^{17}O signal of the sulfonyl oxygen group of LiFSI was up-shifted from 171.15 to 166.35 ppm, indicating that the amount of FSI⁻ anion involved in the solvation-structure increased after the introduction of TFEE into the electrolyte (Fig. S5(a)).

Note S2. Defluorination mechanism of TFEE

Density functional theory (DFT) calculations were used to analyze the defluorination mechanism of TFEE (which contributes to LiF-based SEI formation). As indicated by the reaction diagram of the reductive decomposition of TFEE, the reaction pathway involving 2e^- reduction was thermodynamically favorable and the TFEE was decomposed to C_2H_4 and C_2HOF_4^- (Fig. S19(a)). The LUMO energy levels of TFEE, according to the degree of reduction, validated the occurrence of a 2e^- reduction of TFEE (Fig. S19(b)). The defluorination of the C_2HOF_4^- anion, possible due to interactions with Li^+ -ions, formed LiF (Fig. S19(c)). Thus, interactions with Li^+ -ions significantly influence the defluorination mechanism, transforming the reaction to a kinetically and thermodynamically favorable reaction.

Note S3. Scanning electron microscopy (SEM) morphology after Li deposition on Cu substrate

Fig. S29 shows the surface and cross-sectional SEM images of electrochemically plated Li on a Cu. Despite the presence of compressive forces, Li was electrochemically deposited in a nonuniform size and shape (mainly fibrous) in the LCE, with a void between the electrodeposited Li with a thickness of $41.8\ \mu\text{m}$. LCE showed a low ICE of $\sim 15.3\%$; thus, the electrodeposited Li is possibly composed of active Li and large amounts of LiSFI- and DME-

decomposition byproducts. Moreover, porous lithium deposition increased the surface area of Li, which increased the probability of direct contact between the electrolyte and active Li.³ This may cause severe problems, such as active Li consumption, reduction of the CE, and electrolyte depletion.⁴ Furthermore, thick and resistive Li deposition obstructs the migration of Li⁺-ions, which contributes to the formation of dead Li in an electrochemically isolated state. However, in TFEE containing electrolytes, Li was deposited in a relatively uniform size and shape (mainly particle-like deposition), and there was almost no void between the deposited Li, resulting in a relatively thin Li layer. Due to the deposition of small and densely arranged Li, compact Li deposition was observed in PWSE+LiFMDFB+AgNO₃. Thus, TFEE, LiFMDFB, and AgNO₃ facilitate the formation of a stable SEI, which minimizes undesirable electrolyte decomposition on the Li metal anode.

Note S4. Effect of LiFMDFB and AgNO₃ on the Li metal anode, respectively

SEM images of Li deposition on a Cu in PWSE+LiFMDFB (LiFSI DME/TFEE (1.3 M; 2/8, v%)+1% LiFMDFB) and PWSE+AgNO₃ (LiFSI DME/TFEE (1.3 M; 2/8, v%)+0.05% AgNO₃) were used to analyze the effect of LiFMDFB and AgNO₃ on the Li metal anode further. Without a compressive force, PWSE+LiFMDFB showed dendritic morphology; highly resistive LiF-based SEI formation caused Li deposition along the vertical path, without direct penetration of the SEI (Fig. S30(a) and (b)).⁵ However, in PWSE+AgNO₃, formation of an LiF-Ag based SEI enabled Li deposition through the SEI (lateral growth) (Fig. S30(c) and (d)). With a compressive force (1.3T spacer), due to the effect of pressure, PWSE+LiFMDFB showed nodule-like morphology at the surface and dendritic morphology at the bottom of the deposited Li (Fig. S30(e) and (f)).⁶ However, in PWSE+AgNO₃, compact and particle-like morphology was observed, with/without compressive forces (Fig. S30(g) and (h)). Dendritic morphology was not observed when LiFMDFB and AgNO₃ were applied together, indicating

that AgNO_3 significantly influenced Li deposition.

Note S5. Effect of stable and ion-conductive SEI (LiF+Ag-incorporated SEI) under a high areal-capacity condition

Fig. S31 shows the morphology and inset digital photographs of Li deposition on a Cu with a compressive force, according to different areal-capacities. At a low areal-capacity of 2 mAh cm^{-2} , nonuniform Li deposition occurred in the LCE. At areal-capacities of 6 mAh cm^{-2} and 10 mAh cm^{-2} , SEI-containing deposited Li occupied the marginal space, and no porous parts were observed (Fig. S31(a)). Unlike the LCE, the PWSE showed relatively uniform Li deposition at 2 mAh cm^{-2} . The morphology of deposited Li was maintained relatively well, even at 6 mAh cm^{-2} . However, at 10 mAh cm^{-2} , the deposited Li was partially compressed nonuniformly (Fig. S31(b)). Interestingly, PWSE+LiFMDFB+ AgNO_3 showed completely compact and uniform Li deposition from 2 mAh cm^{-2} to 10 mAh cm^{-2} (Fig. S31(c)). In an environment with relatively low pressurization, the trend shown in Fig. S31(a) was observed (Fig. S32 and S33). Very little Li deposition occurred at 2 mAh cm^{-2} in the LCE; the deposited Li showed a mossy morphology with numerous voids (Fig. S32). Additionally, despite an increased amount of Li deposition on Cu, due to weak adhesion, the Li detached easily from Cu. In the PWSE, relatively large particles were deposited on the Cu substrate. However, at 10 mAh cm^{-2} or higher, dendritic deposition was observed. Systems with a high areal-capacity show larger amounts of Li deposition than those with a low areal-capacity within the same time. Therefore, Li metal-electrolyte interfaces constructed by TFEE are unsuitable for large amounts of Li deposition, which accompanies severe volume changes. A steady and dense deposition of relatively small Li particles was observed in PWSE+LiFMDFB+ AgNO_3 . Notably, its plating overpotential, even under high areal capacities, was lower than that of other electrolytes, since the stable SEI developed by functional additives could withstand the stress accompanied by severe volume

changes (Fig. S33).

Note 6. Optimal amounts of TFEE, LiFMDFB, and AgNO₃ for Li|LiCoO₂ full cell operation

The optimal amounts of TFEE, LiFMDFB, and AgNO₃ for the stable cyclability of Li|LiCoO₂ full cells were determined through electrode-electrolyte interface stabilization. PWSE+LiFMDFB+AgNO₃ shows the best cycle stability due to the enhanced oxidative stability of the electrolyte and construction of an optimal SEI and cathode-electrolyte interface (CEI) by TFEE, LiFMDFB, and AgNO₃. Insufficient TFEE may adversely influence the oxidative stability of the electrolyte, because of the increased possibility of nucleophilic attack with free DME (Fig. S39). Moreover, lean additives may be insufficient for acceptable SEI and CEI generation (Fig. S40).

Table S1. Details of the electrolytes (LCE, PWSE, PWSE+LiFMDFB+AgNO₃, and LHCE)

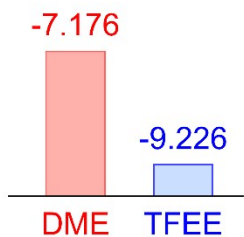
Electrolyte	LCE	PWSE	PWSE +LiFMDFB +AgNO ₃	LHCE
LiFSI (M)	1.3	1.3	1.3	1.3
Solvents	DME	DME/TFEE (2/8, v%)	DME/TFEE (2/8, v%)	DME/TTE (2/8, v%)
Additives	-	-	1% LiFMDFB + 0.05% AgNO ₃	-
Ionic conductivity (mS cm ⁻¹)	17.67	4.34	4.25	3.65
Viscosity (cP)	2.21	5.50	5.65	4.2
Transference number (t _{Li+})	0.528	0.502	0.485	0.325
Li ⁺ diffusion coefficient (m ² s ⁻¹)	4.429 × 10 ⁻⁶	2.803 × 10 ⁻⁶	-	1.58 × 10 ⁻⁶

Table S2. Electrolyte used for testing the Li|LiCoO₂ full cell cyclability

Amount of electrolyte (56.67 μℓ)	
Per a coin cell	E/C ratio
0.0408 g cell ⁻¹	8.5 mg mAh ⁻¹

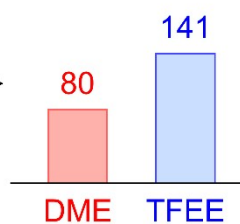
1. Enhanced oxidation stability

HOMO energy level (eV)

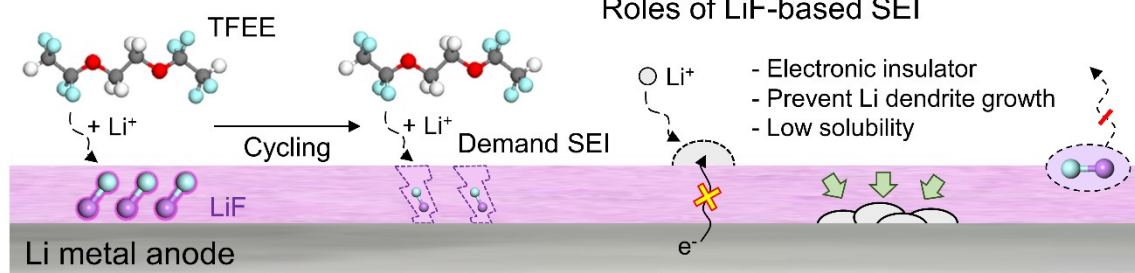


2. Enhanced thermal stability

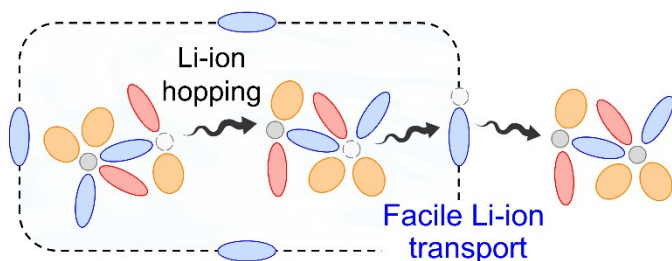
Boiling point (°C)



3. LiF-based SEI formation and demand the crack of SEI during cycling



4. Facile Li-ion transport (Solvation ability)



5. Facile Li-ion desolvation

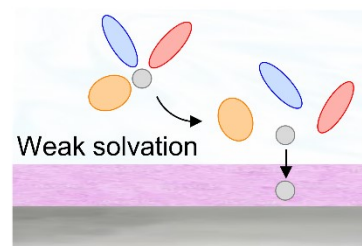


Fig. S1. Beneficial effects of the PWSE structure on battery performance.

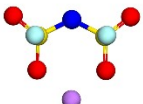
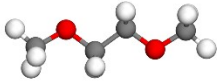
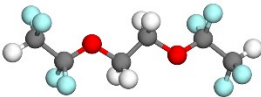
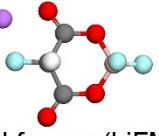
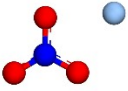
 <p>Li salt (LiFSI)</p>	<ul style="list-style-type: none"> - Easy to be dissociated - Less formation of acidic compounds such as HF - Anion-derived SEI formation on lithium-metal anodes
 <p>Solvent (DME)</p>	<ul style="list-style-type: none"> - High donor number (20.76) for dissociation of lithium salts and additives - Relatively stable toward lithium-metal anodes
 <p>Solvent (TFEE)</p>	<ul style="list-style-type: none"> - Lithium salt dissociation capability (constructing PWSE structure) - Enhanced oxidation stability - High boiling point (141 °C) cf) TTE : 92 °C - Capable of forming LiF-based SEI on lithium-metal anodes
 <p>SEI/CEI former (LiFMDFB)</p>	<ul style="list-style-type: none"> - LiF-based SEI formation on lithium-metal anodes - CEI composed of malonate-induced carbonyl species and electron deficient boron atom trapping radical oxygen species
 <p>SEI former (AgNO₃)</p>	<ul style="list-style-type: none"> - Ag-based SEI on lithium-metal anodes - Uniform lithium deposition, while suppressing lithium dendrite formation

Fig. S2. Reason for choosing LiFSI, DME, TFEE, LiFMDFB, and AgNO₃ for developed electrolyte in the present study.

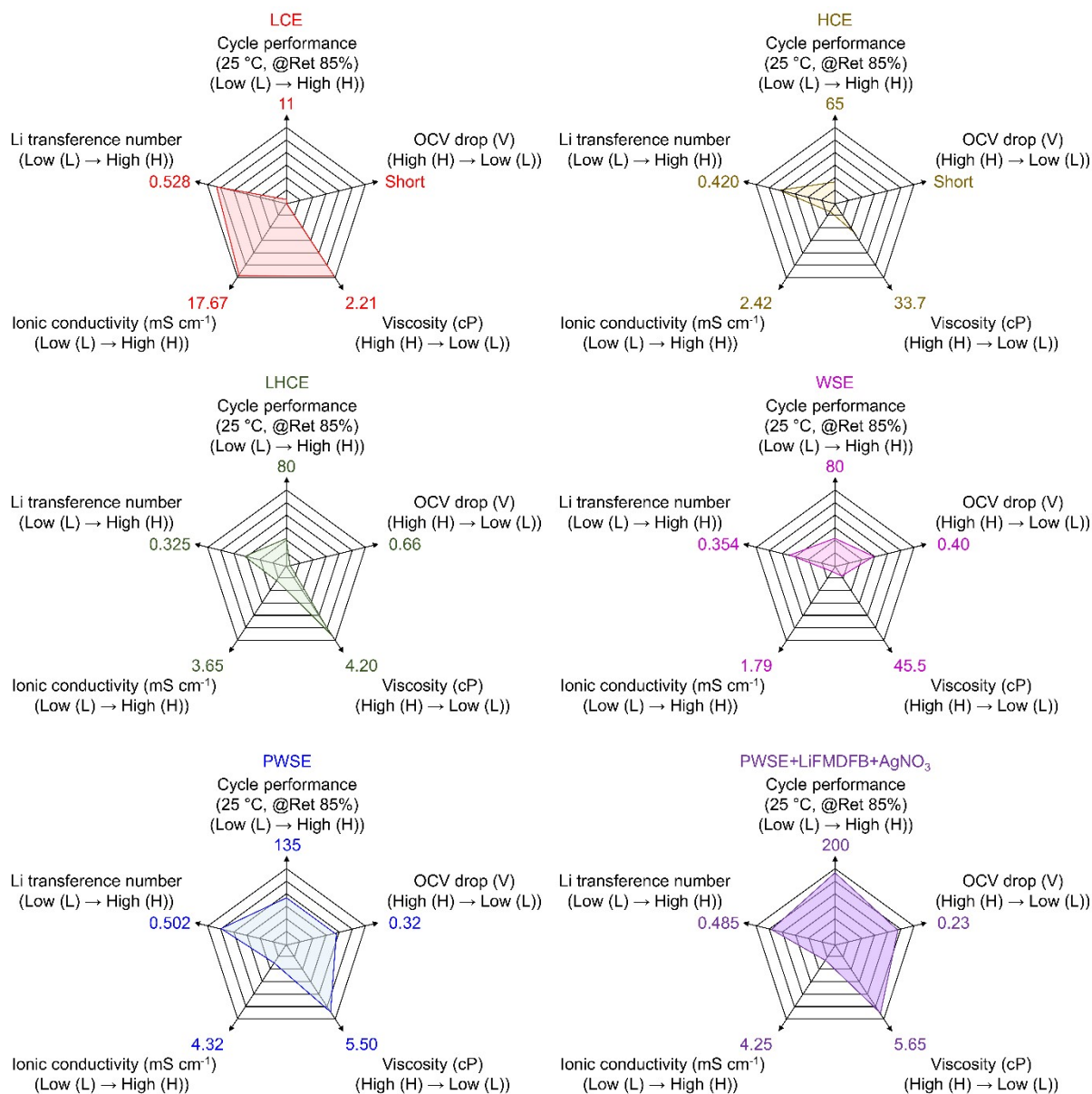


Fig. S3. Comparison of cycle performance at 25 °C, storage performance at 60 °C (open-circuit voltage (OCV) drop), viscosity, ionic conductivity, and Li transference number of LCE, HCE, LHCE, WSE, PWSE, and PWSE+LiFMDFB+AgNO₃. 1.3 M LiFSI DME is labeled as LCE, 4 M LiFSI DME is labeled as HCE, 1.3 M LiFSI DME/TTE (2/8, v%) is labeled as LHCE, 4 M LiFSI DEE is labeled as WSE, 1.3 M LiFSI DME/TFEE (2/8, v%) is labeled as PWSE, and 1.3 M LiFSI DME/TFEE (2/8, v%)+1% LiFMDFB+0.05% AgNO₃ is labeled as PWSE+LiFMDFB+AgNO₃.

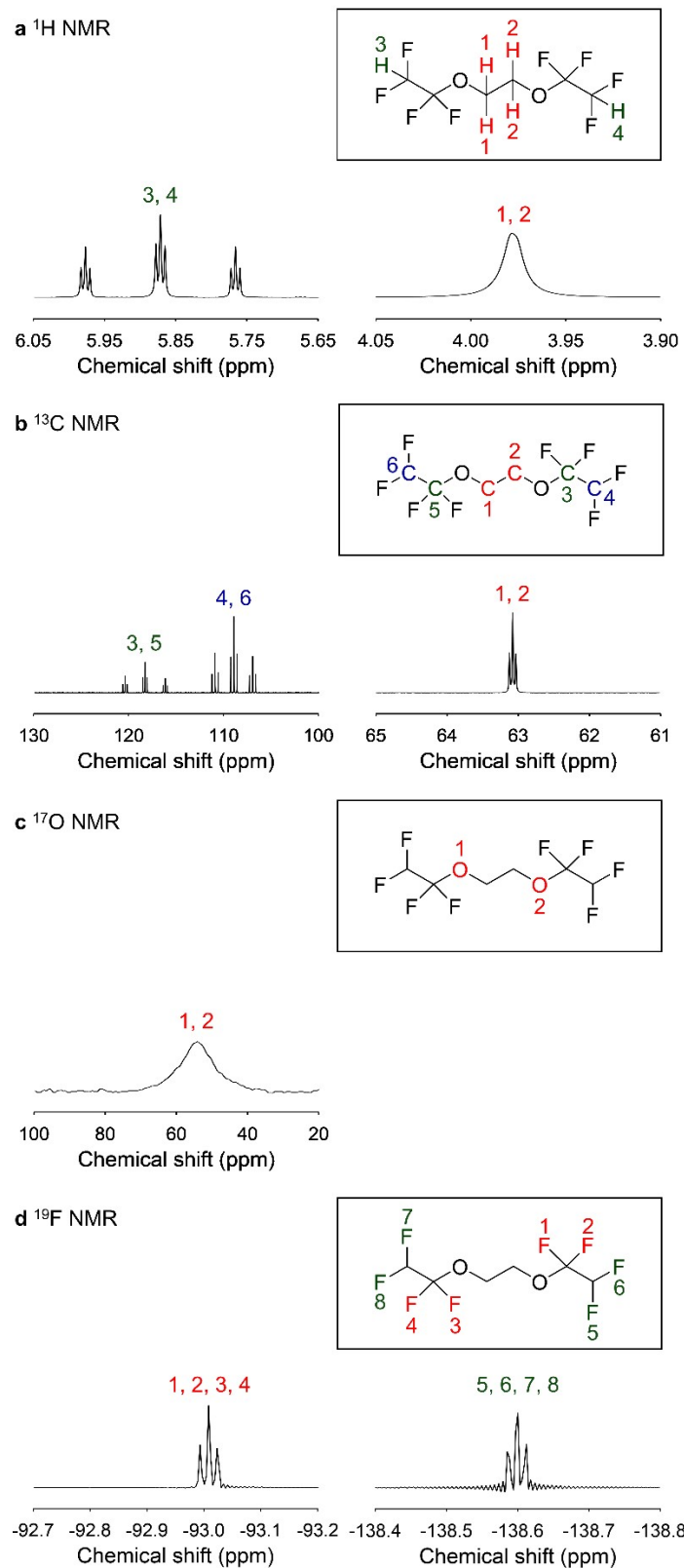


Fig. S4. Chemical composition of TFEE. (a) ^1H , (b) ^{13}C , (c) ^{17}O , and (d) ^{19}F NMR spectra of the TFEE solvent.

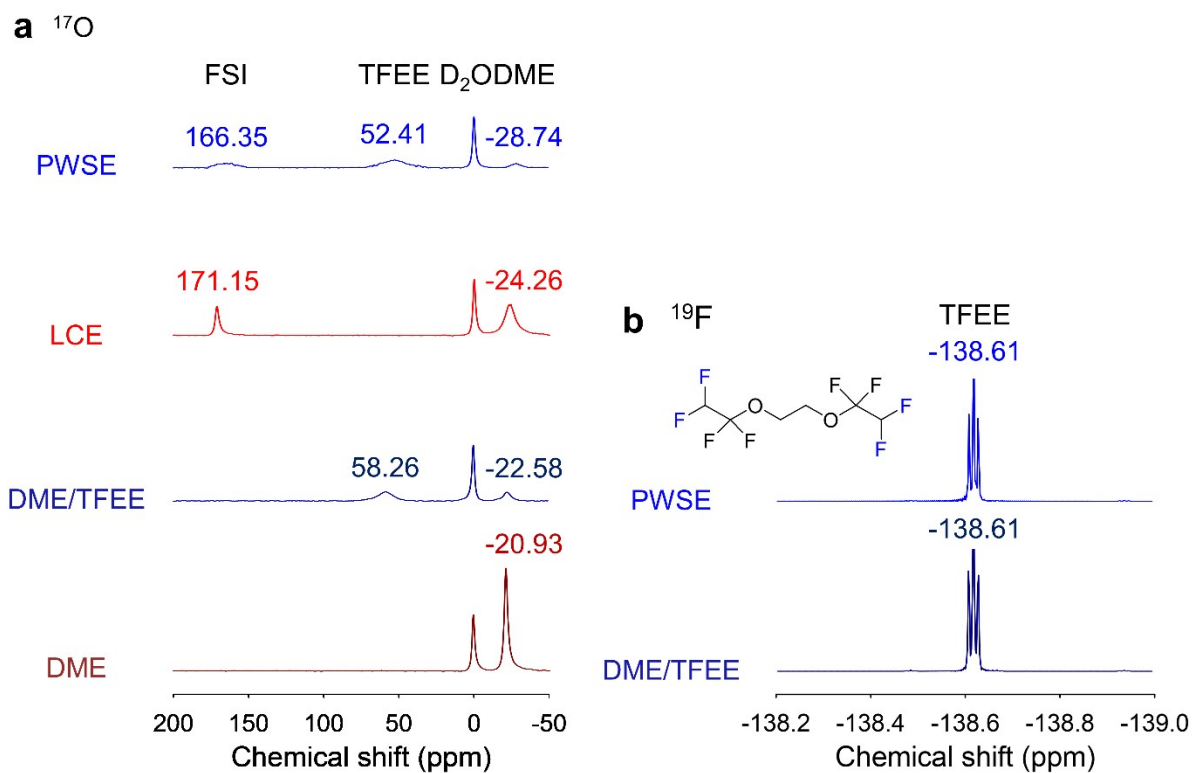


Fig. S5. Comparison of solvation-structures of the LCE and PWSE. (a) ^{17}O NMR spectra of 1,2-dimethoxyethane (DME), DME/TFEE (2/8, v%), and the LCE and PWSE. (b) ^{19}F NMR spectra of DME/TFEE (2/8, v%) and the PWSE.

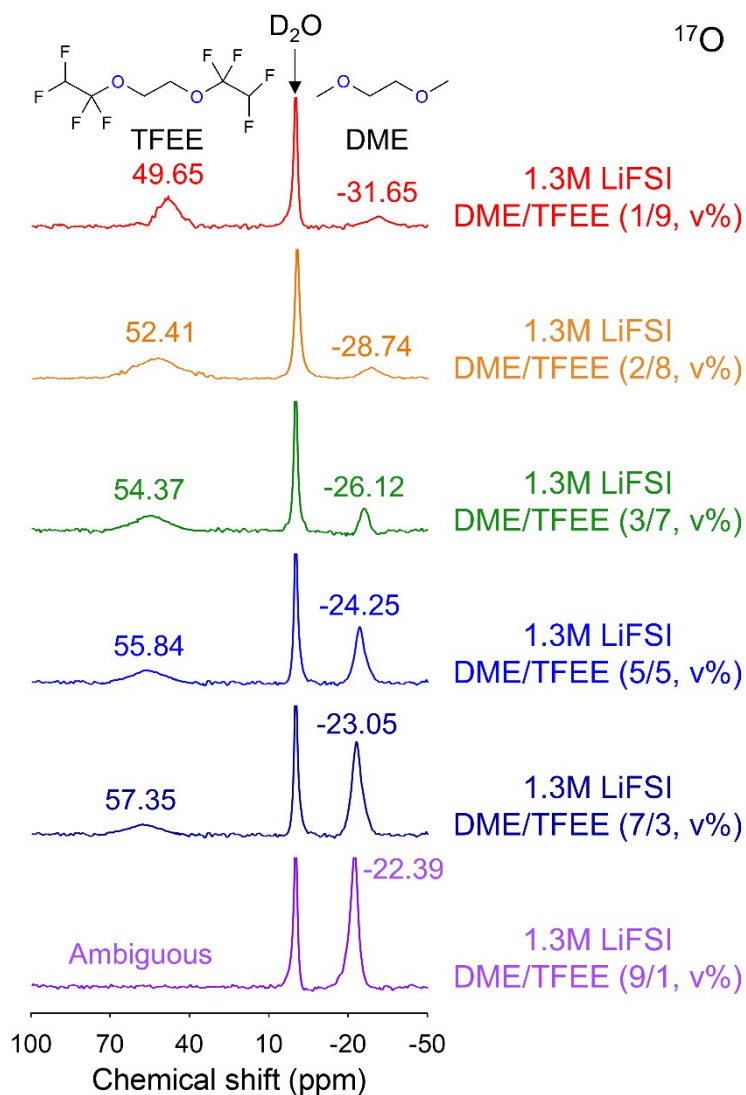


Fig. S6. ^{17}O NMR spectra of 1.3 M LiFSI DME/TFEE (1/9, v%), 1.3 M LiFSI DME/TFEE (2/8, v%), 1.3 M LiFSI DME/TFEE (3/7, v%), 1.3 M LiFSI DME/TFEE (5/5, v%), 1.3 M LiFSI DME/TFEE (7/3, v%), and 1.3 M LiFSI DME/TFEE (9/1, v%).

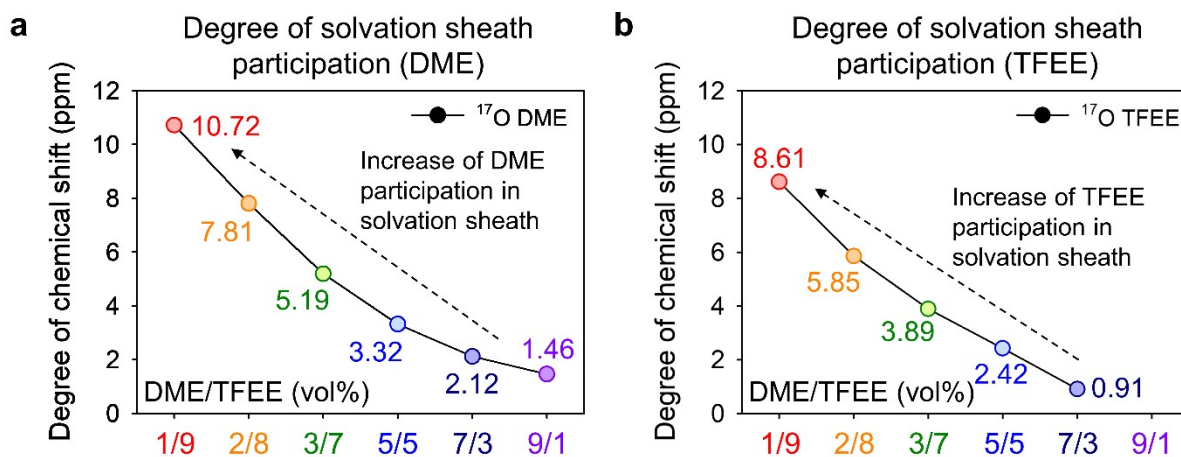


Fig. S7. Degree of chemical shift of (a) DME and (b) TFEE in 1.3 M LiFSI DME/TFEE (1/9, v%; denoted by 1/9), 1.3 M LiFSI DME/TFEE (2/8, v%; denoted by 2/8), 1.3 M LiFSI DME/TFEE (3/7, v%; denoted by 3/7), 1.3 M LiFSI DME/TFEE (5/5, v%; denoted by 5/5), 1.3 M LiFSI DME/TFEE (7/3, v%; denoted by 7/3), and 1.3 M LiFSI DME/TFEE (9/1, v%; denoted by 9/1).

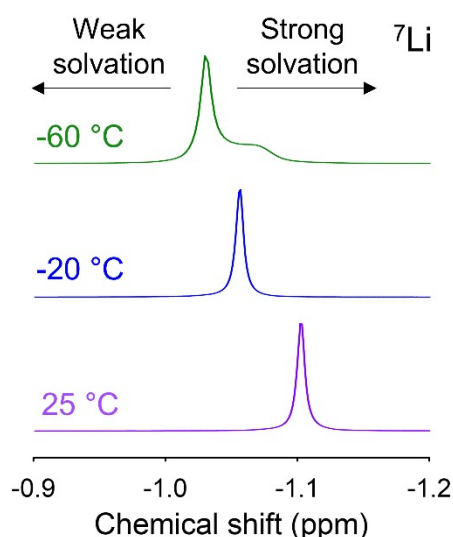


Fig. S8. ^7Li NMR spectra of PWSE (1.3M LiFSI DME/TFEE (2/8, v%)) at 25 °C, -20 °C, and -60 °C.

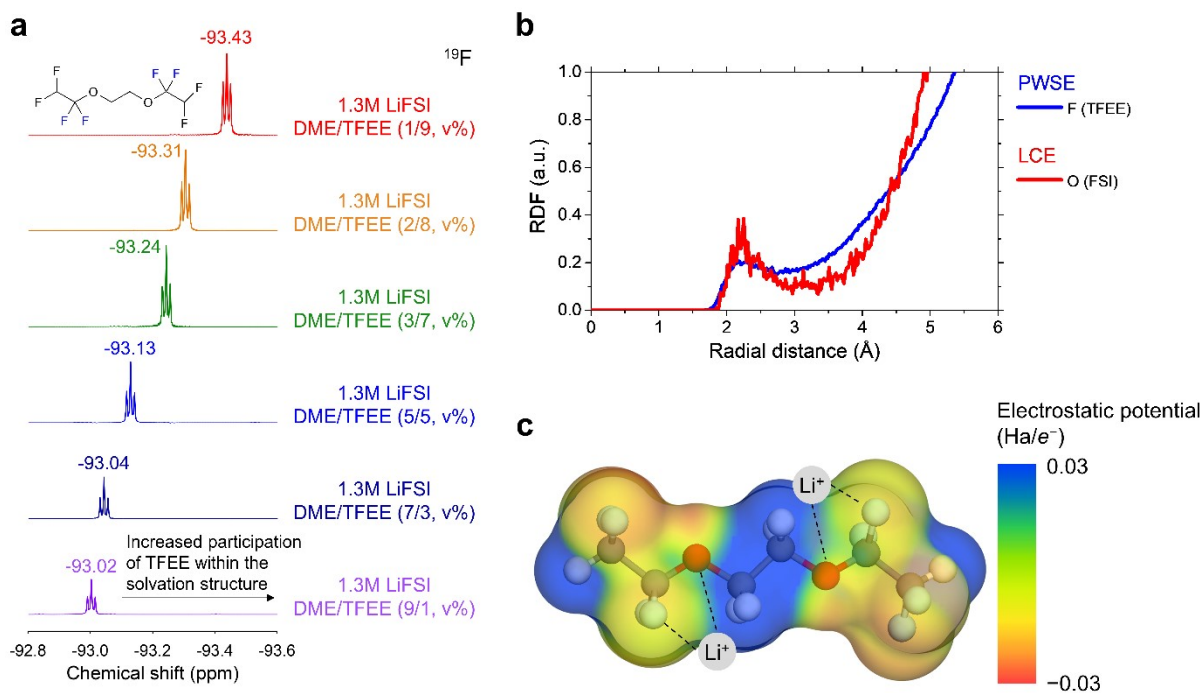


Fig. S9. (a) ¹⁹F NMR spectra of 1.3 M LiFSI DME/TFEE (1/9, v%), 1.3 M LiFSI DME/TFEE (2/8, v%), 1.3 M LiFSI DME/TFEE (3/7, v%), 1.3 M LiFSI DME/TFEE (5/5, v%), 1.3 M LiFSI DME/TFEE (7/3, v%), and 1.3 M LiFSI DME/TFEE (9/1, v%). (b) Radial distribution function (RDF) results of TFEE (oxygen and fluorine atoms) and FSI anion (oxygen atoms) with respect to Li⁺-ions in PWSE and LCE conditions. The inset figure is the enlarged RDF result of TFEE (oxygen atoms). (c) Electrostatic potential result of TFEE molecule.

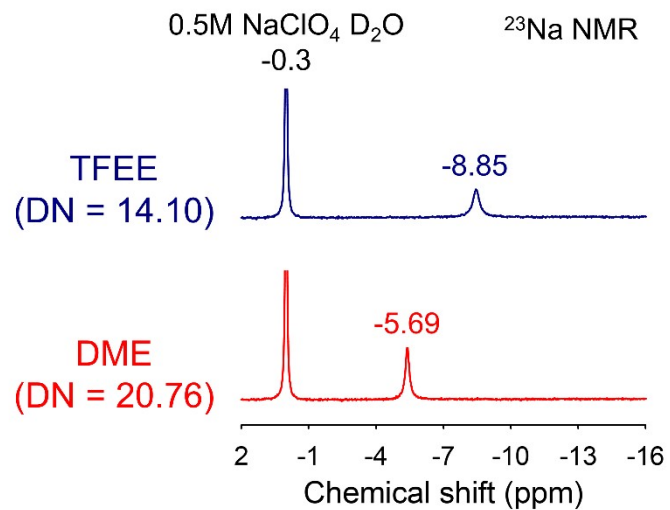


Fig. S10. DN of (a) DME and (b) TFEE.

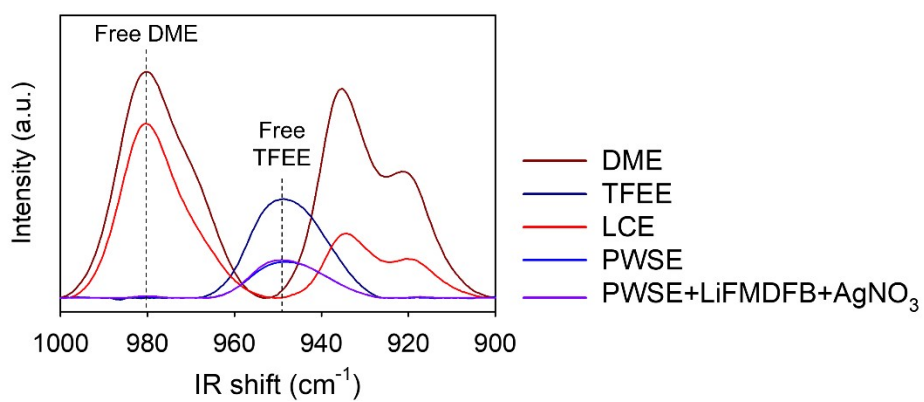


Fig. S11. FT-IR spectra of the solvents (DME and TFEE) and electrolytes (LCE, PWSE, and PWSE+LiFMDFB+AgNO₃) used in this study.

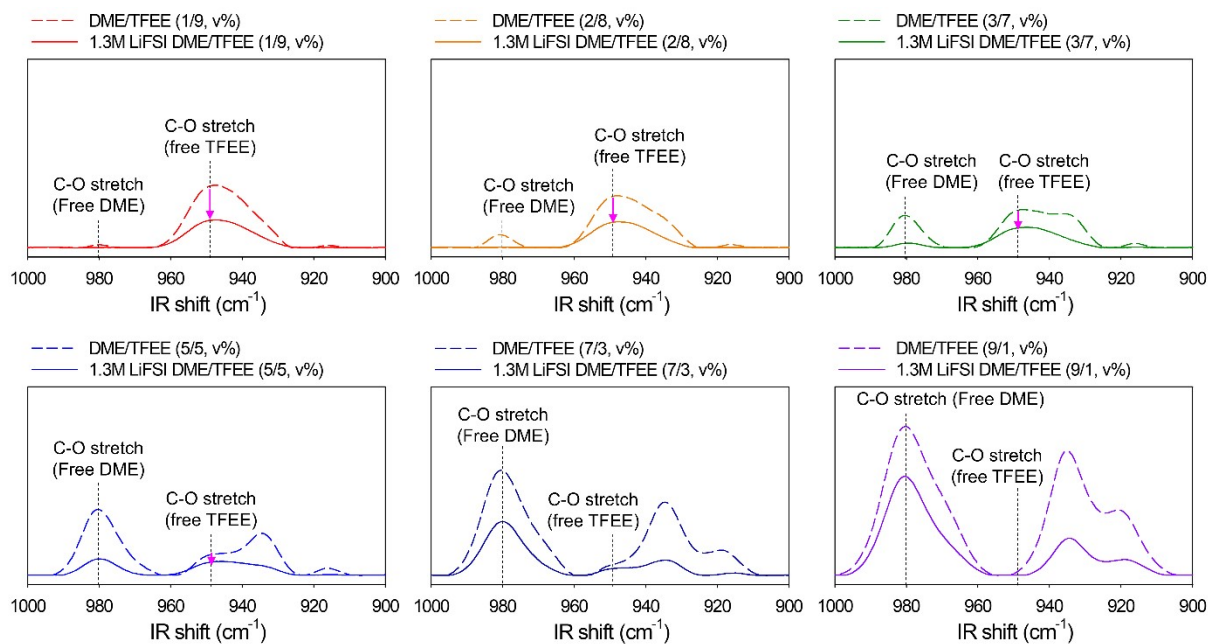


Fig. S12. FT-IR spectra based on the solvent ratio of DME and TFEE within the electrolyte, as well as the presence of lithium salt.

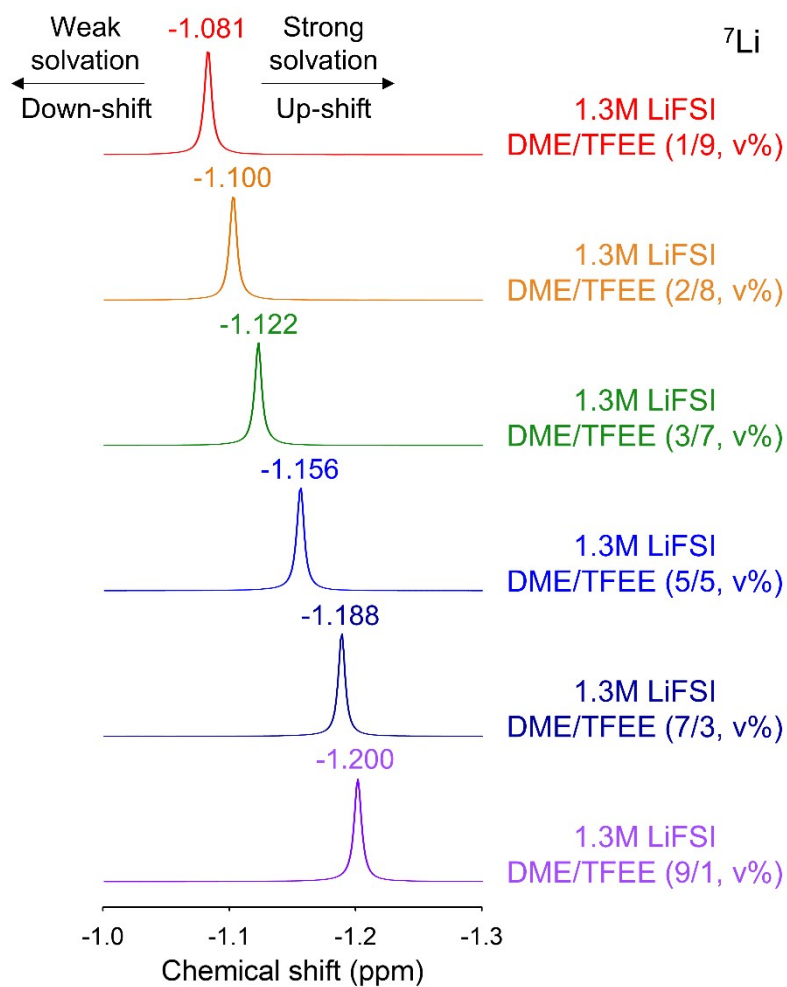
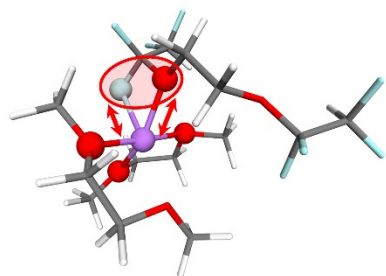
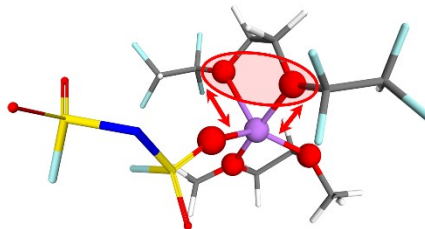


Fig. S13. ⁷Li NMR spectra of 1.3 M LiFSI DME/TFEE (1/9, v%), 1.3 M LiFSI DME/TFEE (2/8, v%), 1.3 M LiFSI DME/TFEE (3/7, v%), 1.3 M LiFSI DME/TFEE (5/5, v%), 1.3 M LiFSI DME/TFEE (7/3, v%), and 1.3 M LiFSI DME/TFEE (9/1, v%).

Li \leftrightarrow F & O atoms in TFEE



Li \leftrightarrow O atoms in TFEE



Li \leftrightarrow F atom in TFEE

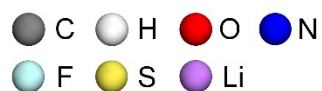
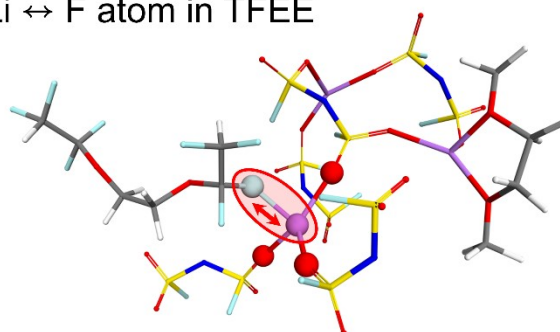


Fig. S14. Li-coordinated molecular structures in the PWSE. Only the coordinated structures including the TFEE molecule are shown. The highlighted (circled) regions indicate interactions of the Li⁺-ion with the TFEE molecule.

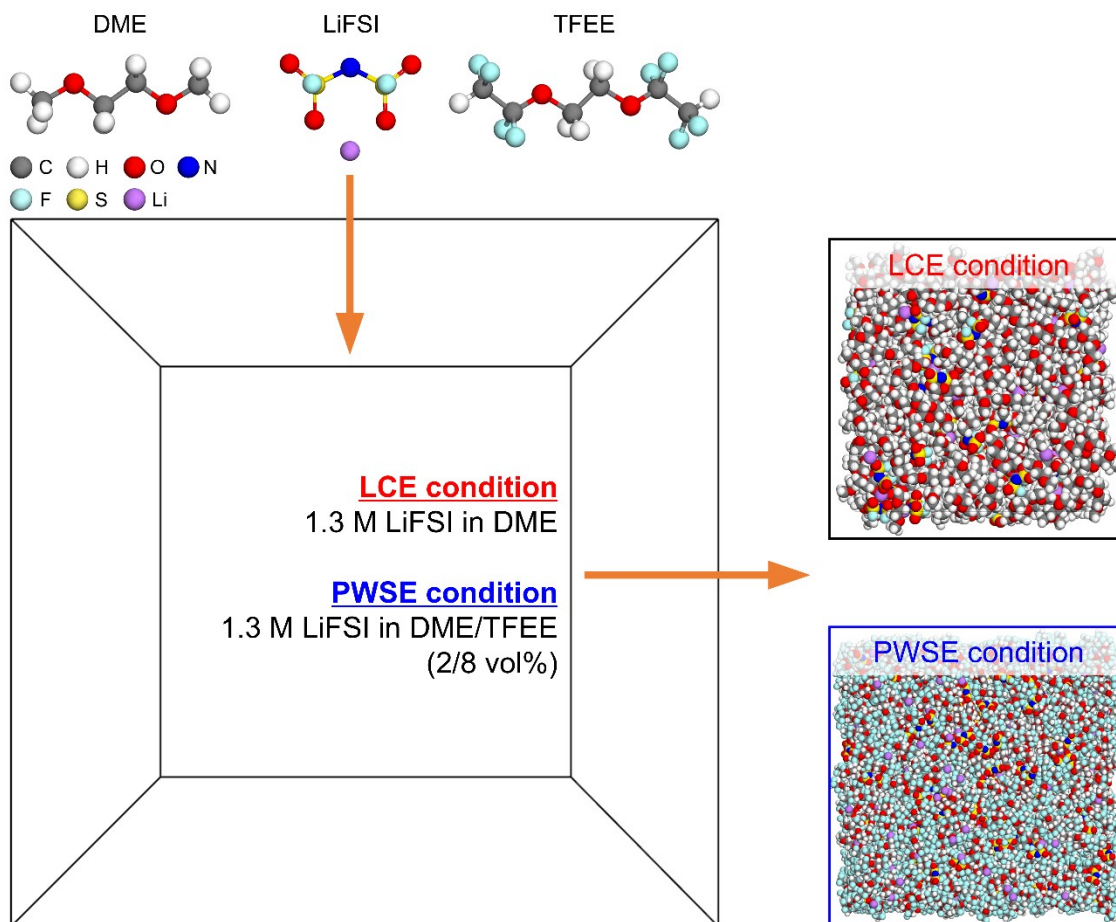


Fig. S15. Model systems for molecular dynamics (MD) simulations considering two types of electrolyte conditions (namely, the LCE and PWSE). For the LCE condition, the number of DME and LiFSI molecules are 500 and 68, respectively. For the PWSE condition, the number of DME, TFEE, and LiFSI molecules are 500, 1168, and 338, respectively.

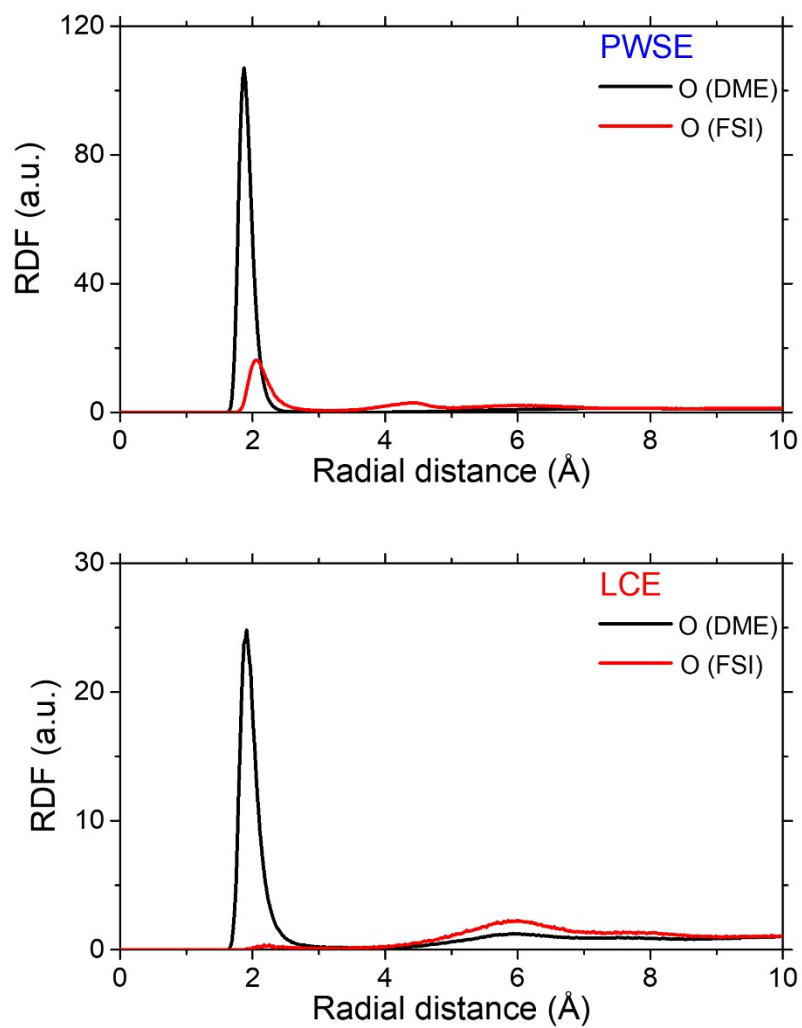


Fig. S16. Radial distribution function (RDF) results of DME (oxygen atoms) and FSI anion (oxygen atoms) with respect to Li^+ -ions in PWSE and LCE conditions.

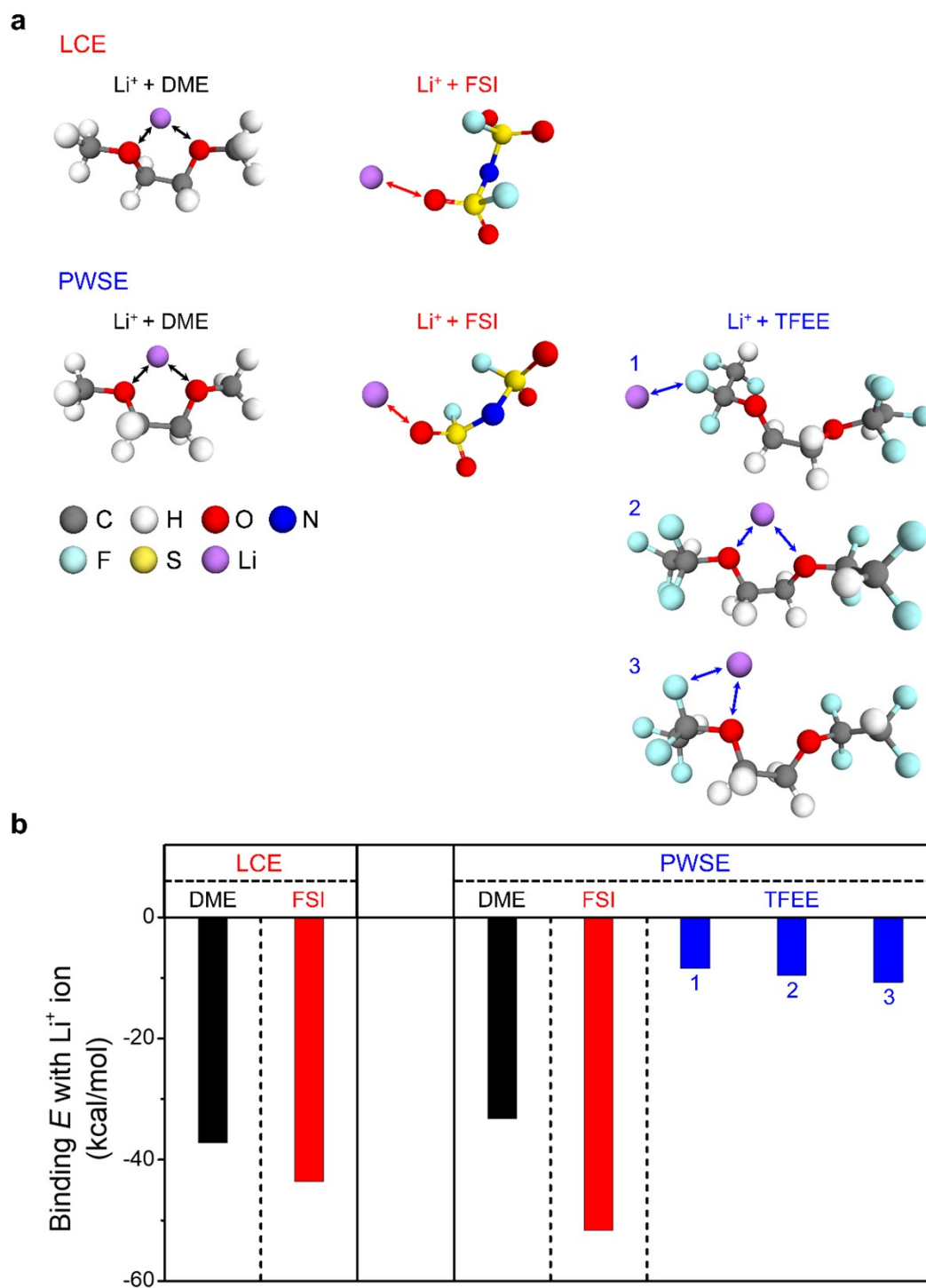


Fig. S17. (a) Molecular structures for calculating the binding energies of the Li⁺-ion in the LCE and PWSE. Each molecular structure is obtained from the results of MD simulations. (b) Binding energies of the Li⁺-ion in the LCE and PWSE.

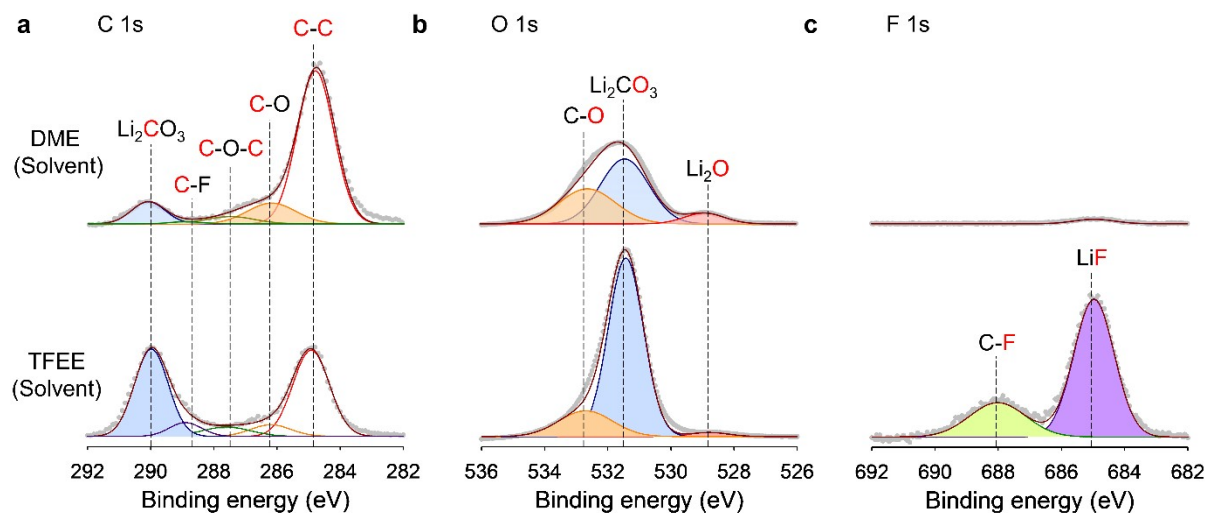


Fig. S18. Construction of LiF-rich solid-electrolyte interphase (SEI) on Li metal anodes by TFEE. (a) C 1s, (b) O 1s, and (c) F 1s XPS profiles of Li metal anodes (size: 15 μm) after being kept in contact with DME (solvent) and TFEE (solvent) for 3 days at 25 $^\circ\text{C}$.

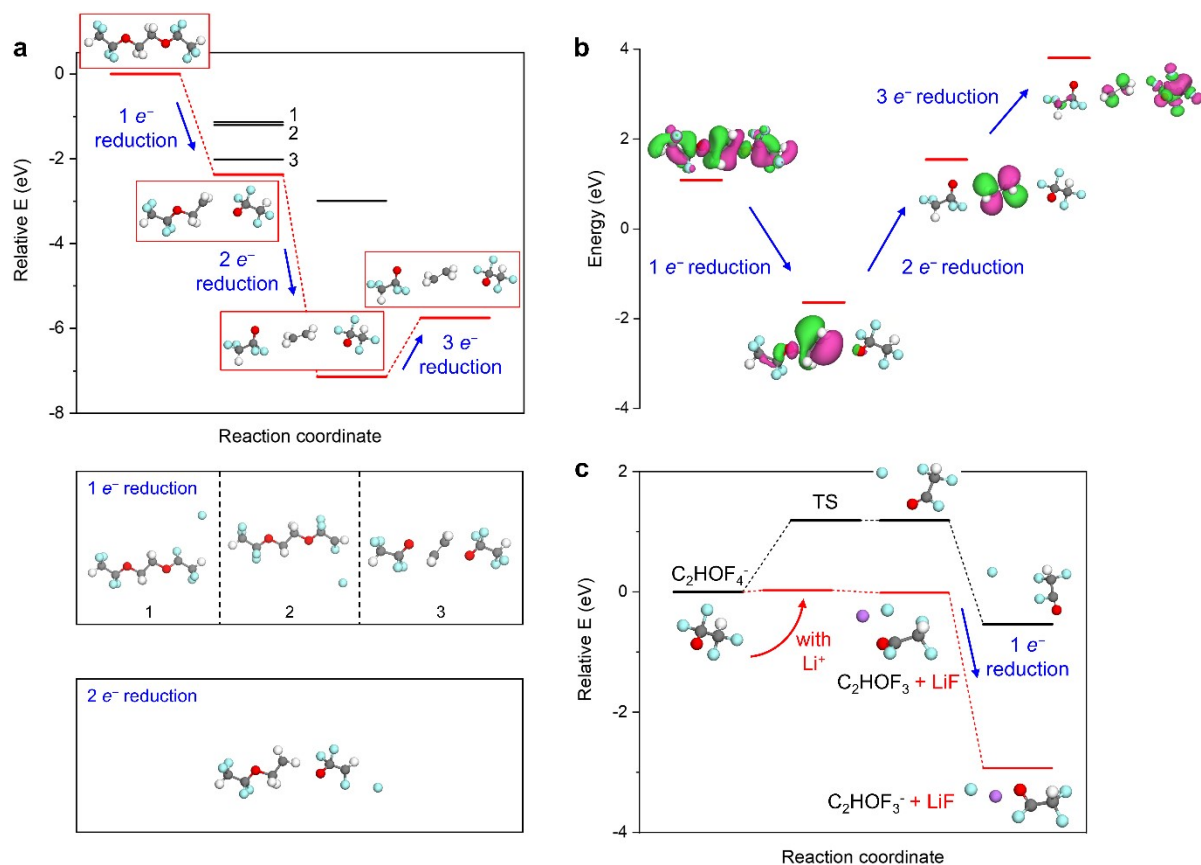


Fig. S19. (a) Reaction diagram of the reductive decomposition of TFEE according to the degree of reduction. Red colored boxes indicate the most thermodynamically favorable molecular structures, black colored boxes indicate the other decomposed configurations, and the label ‘e⁻’ indicates an electron. (b) Lowest unoccupied molecular orbital (LUMO) energy level diagram of TFEE that is shown in the red colored boxes in (a). The isovalue of the orbital is 0.03 e/Å³. (c) Reaction diagram of the defluorination of the C₂HOF₄⁻ anion with and without interacting with Li⁺-ions.

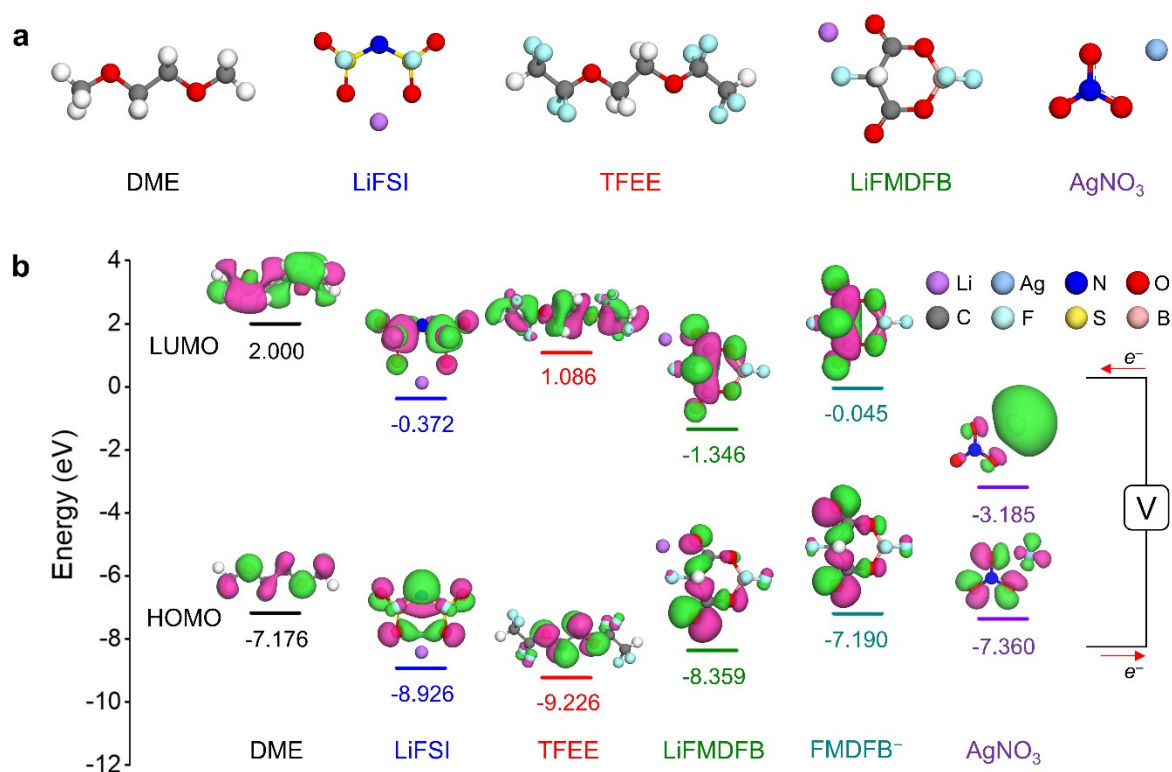


Fig. S20. (a) Molecular structures of the salt (LiFSI), solvents (DME and TFEE), and additives LiFMDFB, FMDFB⁻, and AgNO₃. (b) HOMO|LUMO energy level diagrams of the investigated salt (LiFSI), solvents (DME and TFEE), and additives (LiFMDFB and AgNO₃). The isovalue of the orbital is 0.03 e/Å³. The label ‘e⁻’ indicates an electron.

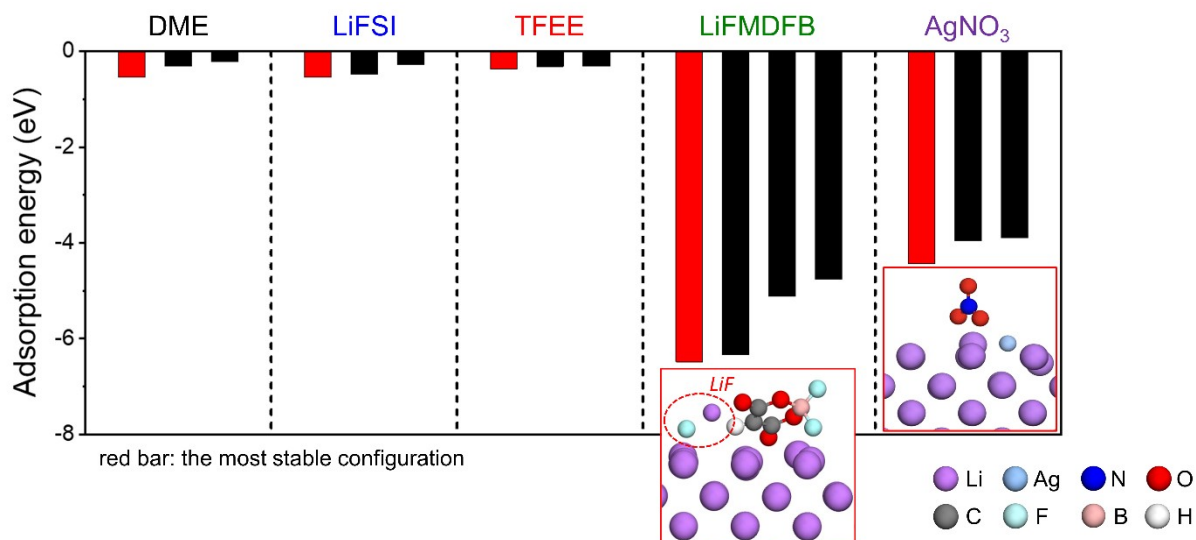


Fig. S21. Adsorption energies of the investigated salt (LiFSI), solvents (DME and TFEE), and additives (LiFMDFB and AgNO₃) on the Li (100) surface, which is the most stable Li metal surface.⁷ The Li surface is constructed by 5×4 supercells of Li surface unit cells. There are seven Li layers in the surface system and the bottom two layers are constrained. The vacuum spacing of the surface system is greater than 20 Å. Red colored bars indicate the most strongly adsorbed cases among the different configurations of each molecule on the Li (100) surface. The FMDFB anion can be defluorinated on the Li surface.

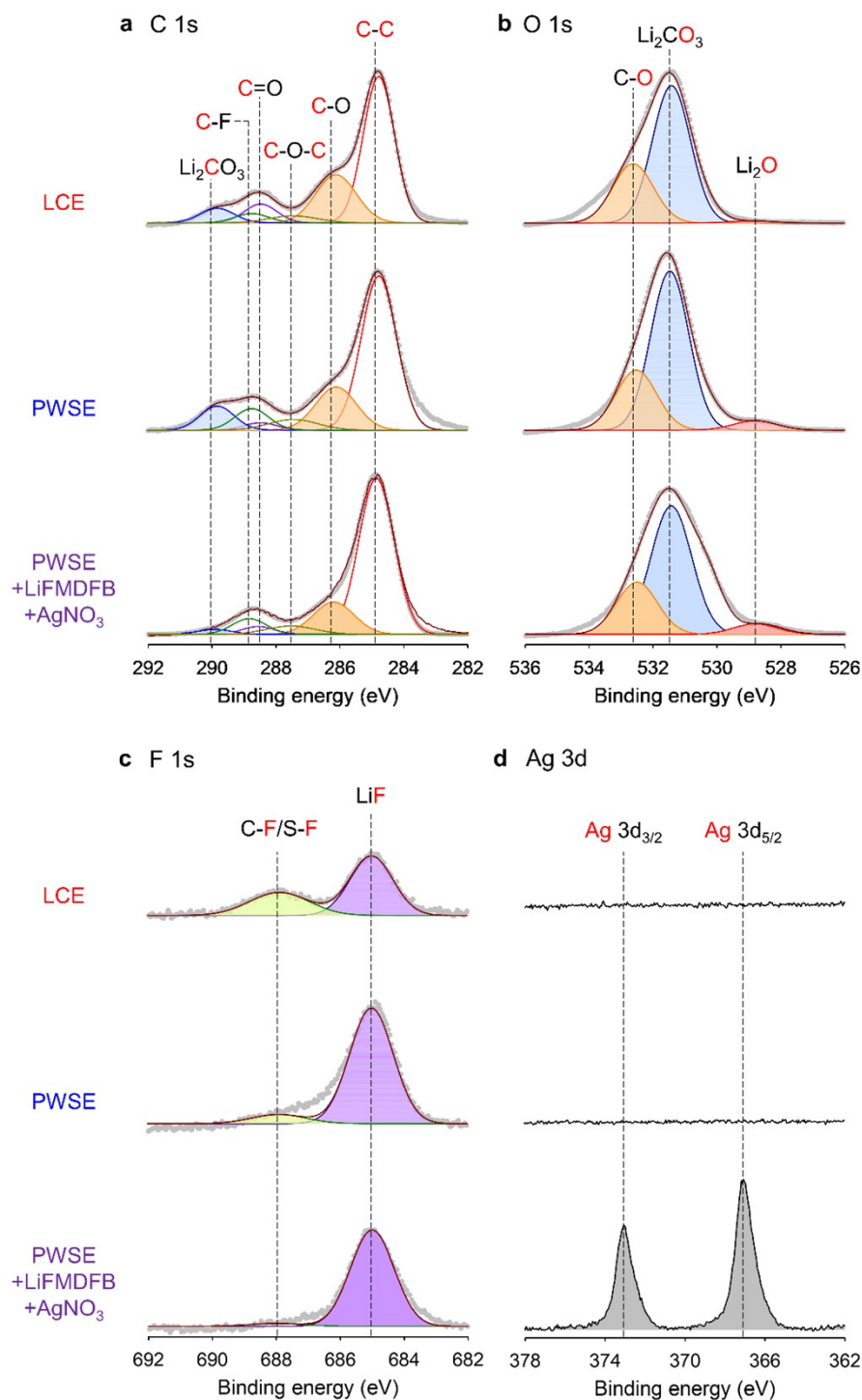


Fig. S22. Surface chemistry of Li metal anodes retrieved from Li|LiCoO₂ full cells precycled with the LCE, PWSE, and PWSE+LiFMDFB+AgNO₃. (a) C 1s, (b) O 1s, (c) F 1s, and (d) Ag 3d XPS profiles of a Li metal anode after precycling at 25 °C.

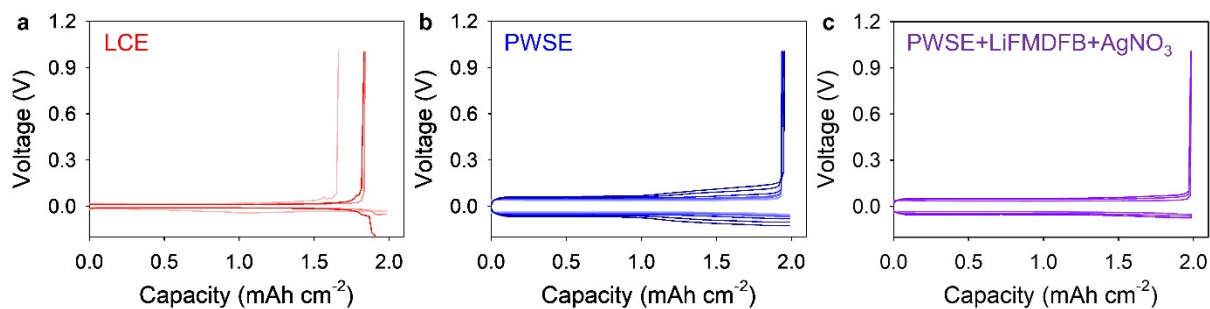


Fig. S23. Electrochemical characteristics of Li|Cu cells. Voltage profiles of Li|Cu cells cycled with the (a) LCE, (b) PWSE, and (c) PWSE+LiFMDFB+AgNO₃ at 25 °C.

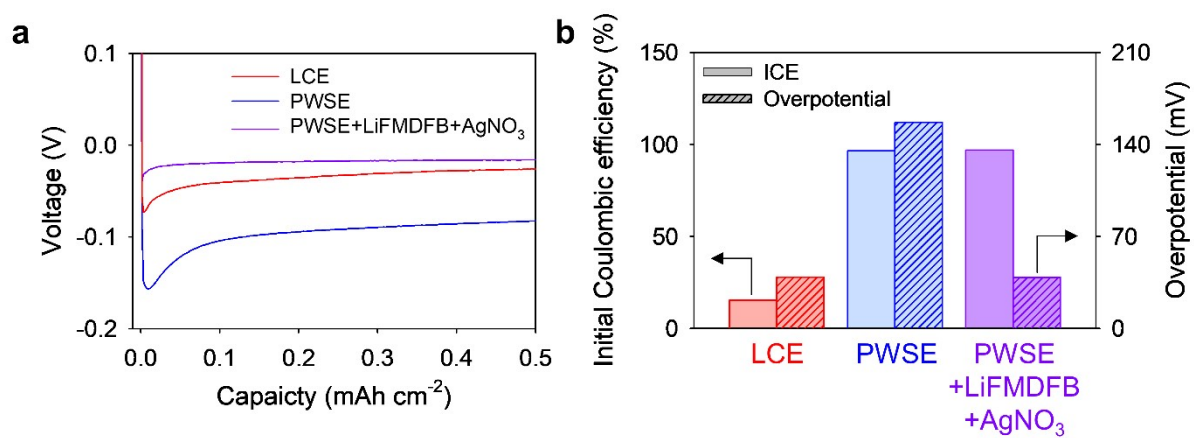


Fig. S24. (a) Magnified voltage profiles of initial Li plating in Li|Cu cells. (b) Comparison of the initial Coulombic efficiency (ICE) and initial plating overpotential of Li|Cu cells.

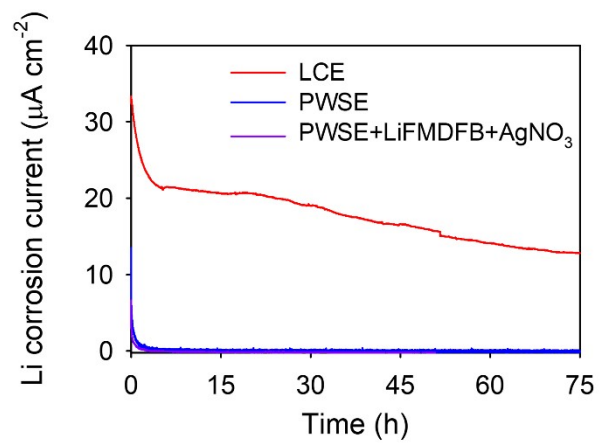


Fig. S25. Li corrosion test of Li|Cu cells at 0 V vs. Li/Li⁺, 75 h after precycling at 25 °C.

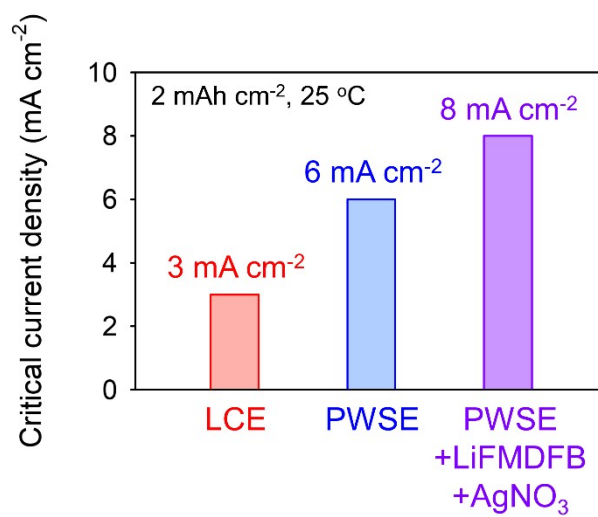


Fig. S26. Critical current density (CCD) of the electrolytes tested by Li|Li cells with an areal-capacity of 2 mAh cm⁻².

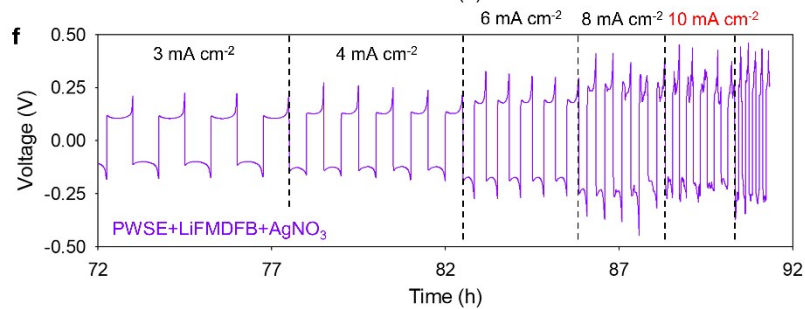
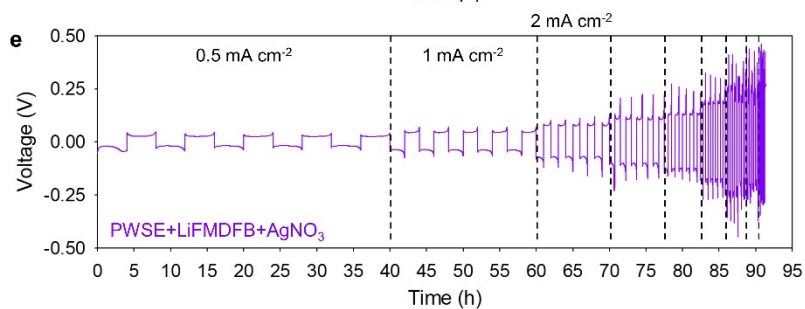
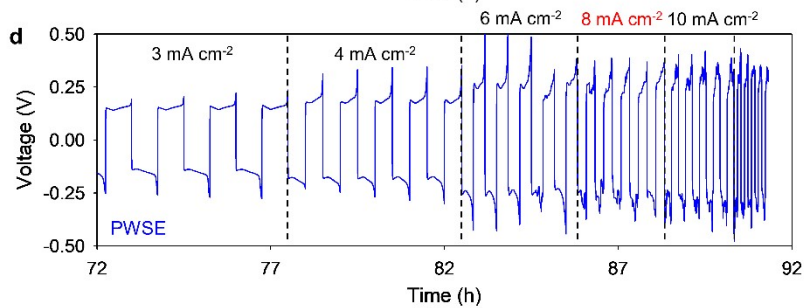
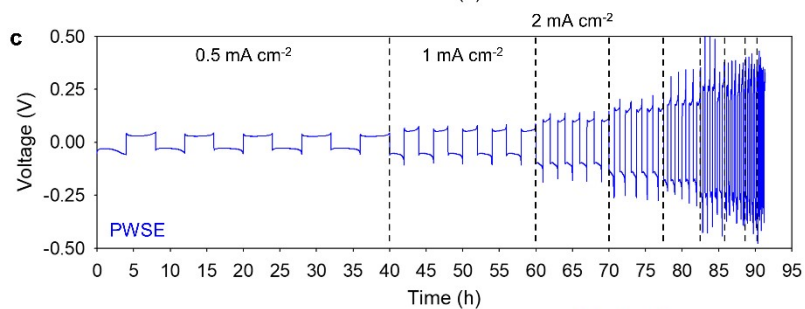
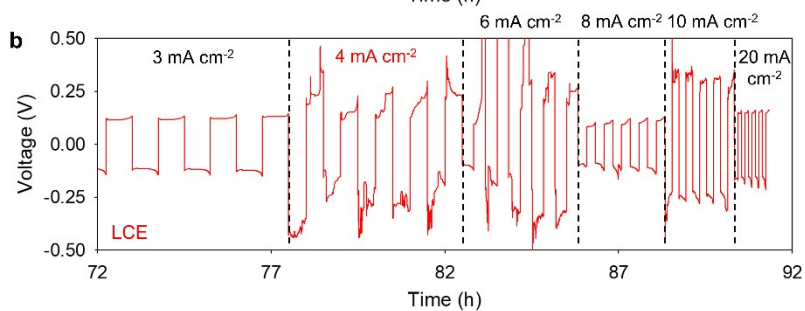
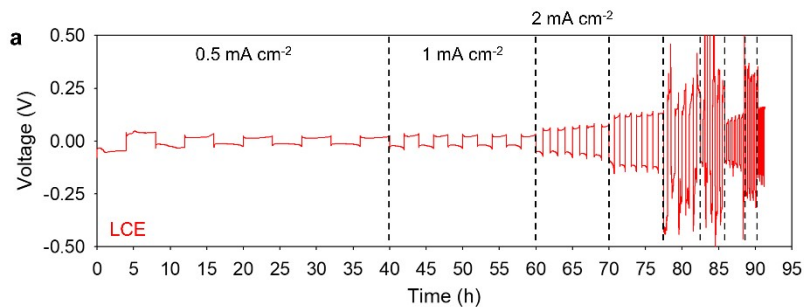


Fig. S27. Electrochemical performances of Li|Li cells. Voltage profiles of a CCD test with the (a-b) LCE, (c-d) PWSE, and (e-f) PWSE+LiFMDFB+AgNO₃ at current densities from 0.5 mA cm⁻² to 10 mA cm⁻².

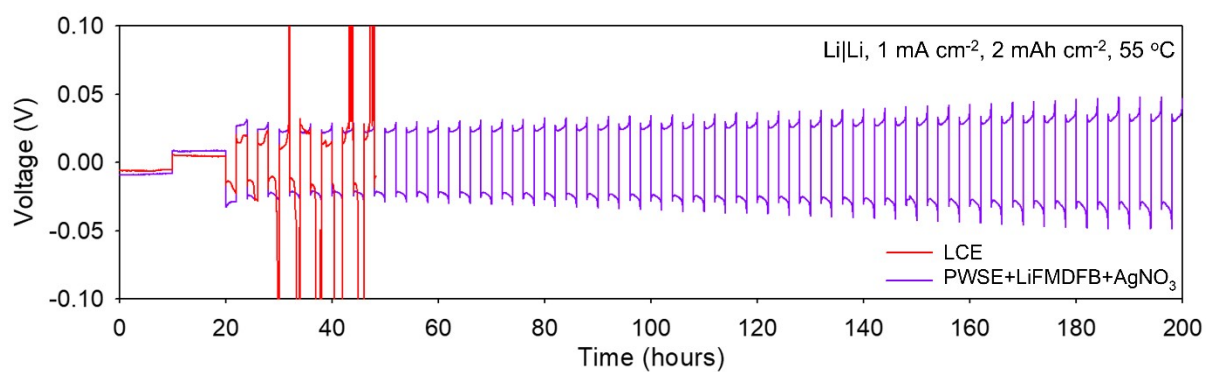


Fig. S28. Voltage profiles of Li|Li symmetric cells at 1 mA cm⁻², 2 mAh cm⁻², and 55 °C.

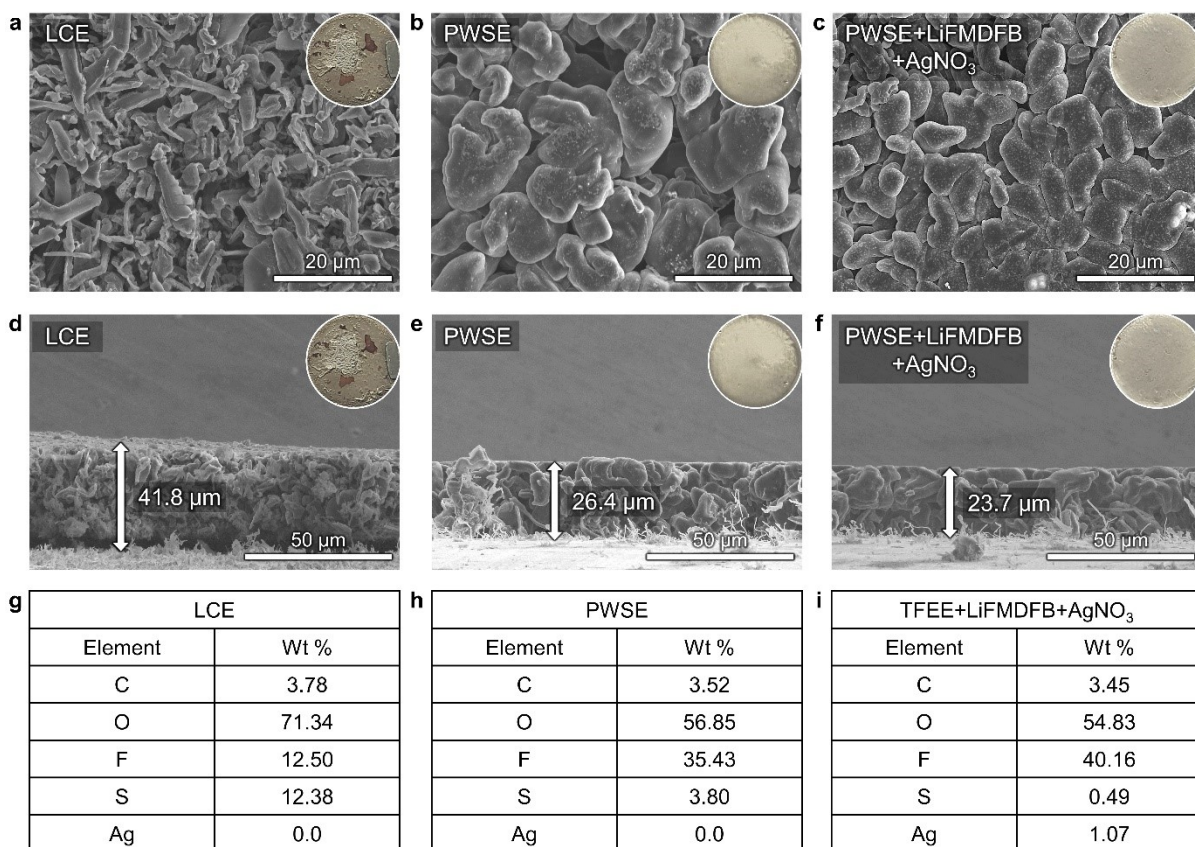


Fig. S29. Surface morphologies and digital images of Li deposited on Cu with the (a) LCE, (b) PWSE, and (c) PWSE+LiFMDFB+AgNO₃. Cross-sectional SEM images of the Li metal after plating on Cu with the (d) LCE, (e) PWSE, and (f) PWSE+LiFMDFB+AgNO₃. Energy dispersive spectrometer analysis of Li deposited on Cu with the (g) LCE, (h) PWSE, and (i) PWSE+LiFMDFB+AgNO₃ electrolytes. All the analyses are conducted using a 2016 coin-cell with a compressive force (1.0T spacer). A foil-type 20 μm Li metal anode was used, and the areal-capacity of the spent Li as a counter electrode was 2 mAh cm⁻².

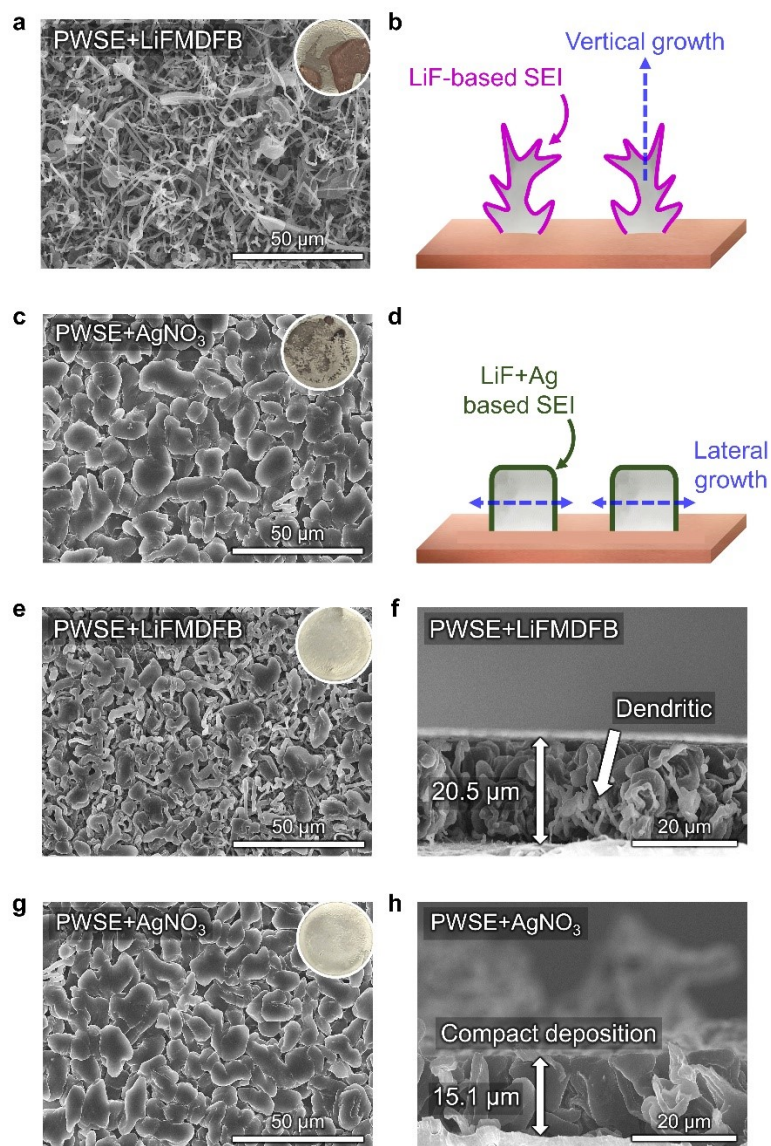


Fig. S30. Surface morphologies and digital images of Li deposited on Cu with the (a) PWSE+LiFMDFB and (c) PWSE+AgNO₃ obtained by SEM, and the corresponding probable mechanisms of Li deposition in the (b) PWSE+LiFMDFB and (d) PWSE+AgNO₃ during Li plating without a compressive force (0.5T spacer). Surface and cross-sectional SEM images of the Li metal after plating on Cu in the presence of a compressive force (1.3T spacer) with the (e-f) PWSE+LiFMDFB and (g-h) PWSE+AgNO₃. A foil-type 20 μm Li metal anode was used and the areal-capacity of the spent Li as a counter electrode was 2 mAh cm⁻² (theoretical thickness : 10 μm).

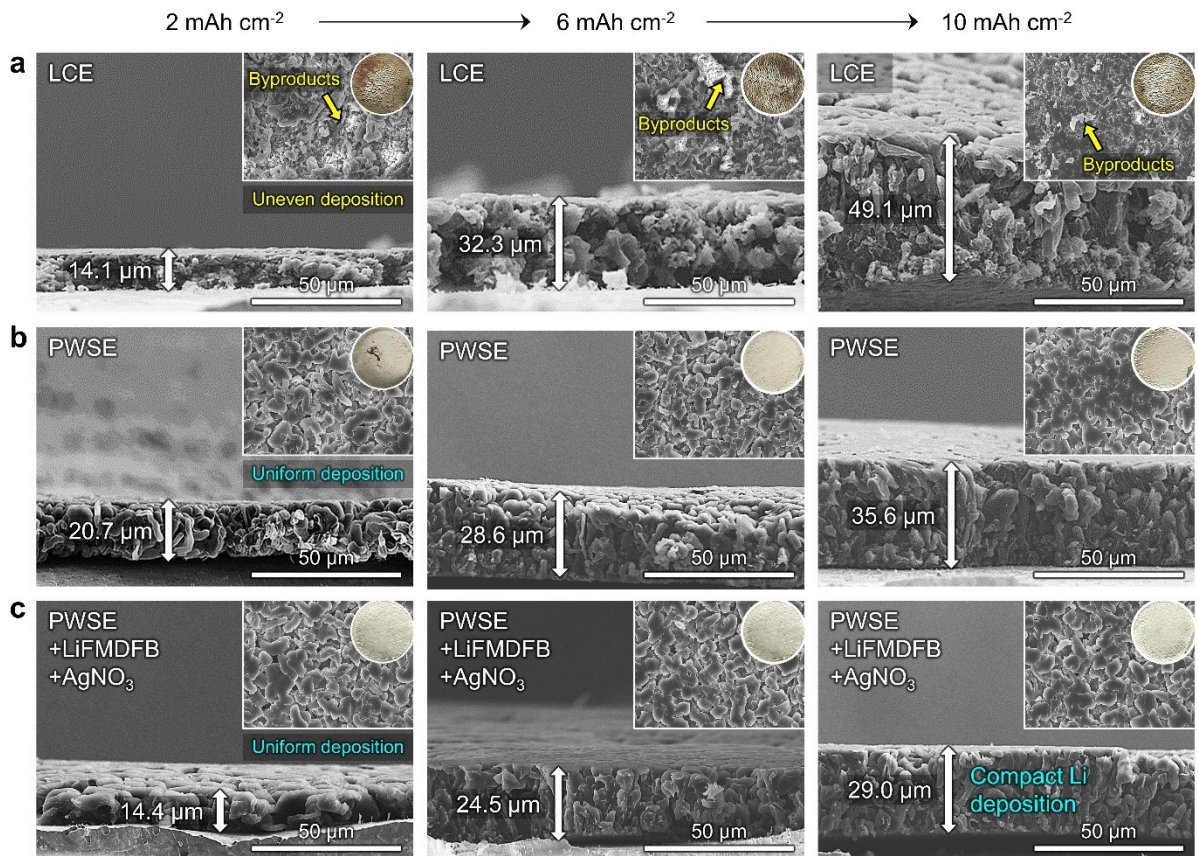


Fig. S31. Cross-sectional, surface morphologies and inset digital images of Li deposited on Cu with the (a) LCE, (b) PWSE, and (c) PWSE+LiFMDFB+AgNO₃ with areal-capacities of 2 mAh cm⁻², 6 mAh cm⁻², and 10 mAh cm⁻². All the analyses are conducted using a 2032 Li|Cu coin-cell with a compressive force (1.3T spacer). A foil-type 200 μm Li metal anode was used and the C-rate for Li plating was C/10.

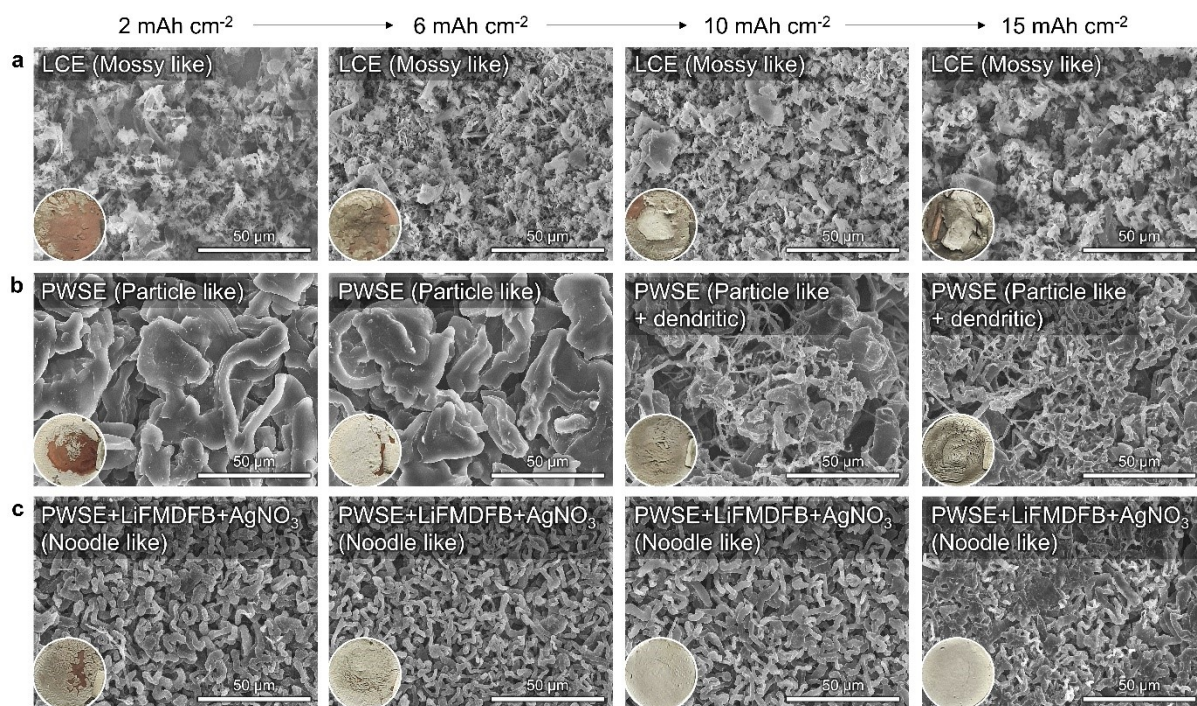


Fig. S32. Surface morphologies and inset digital images of Li deposited on Cu substrates with the (a) LCE, (b) PWSE, and (c) PWSE+LiFMDFB+AgNO₃ with different areal-capacities (2 mAh cm^{-2} , 6 mAh cm^{-2} , 10 mAh cm^{-2} , and 15 mAh cm^{-2}). All the analyses are conducted using a 2016 coin-cell without a compressive force (0.5T spacer). A foil-type $200 \text{ }\mu\text{m}$ Li metal anode was used and the C-rate for Li plating was C/10.

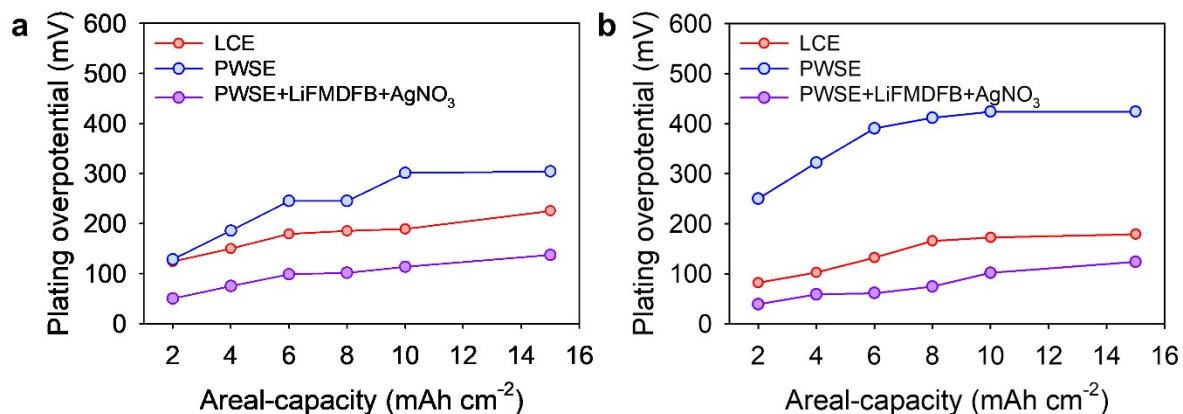


Fig. S33. Comparison of the plating overpotentials under various areal-capacities (2 mAh cm⁻², 4 mAh cm⁻², 6 mAh cm⁻², 8 mAh cm⁻², 10 mAh cm⁻², and 15 mAh cm⁻²) in the LCE, PWSE, and PWSE+LiFMDFB+AgNO₃ with a (a) compressive force (1.3T spacer) and (b) without a compressive force (0.5T spacer).

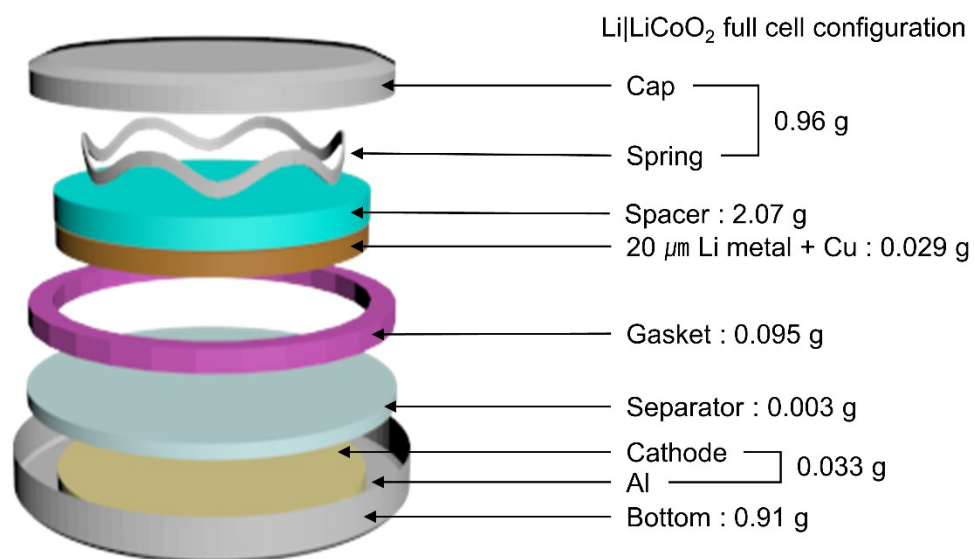


Fig. S34. Schematic illustration of Li|LiCoO₂ full cell configuration.

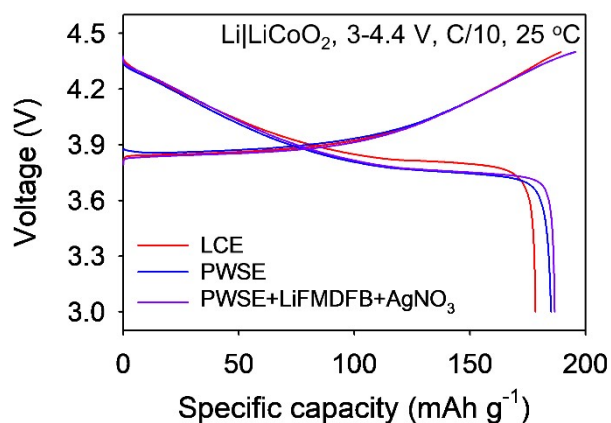


Fig. S35. Voltage profiles of Li|LiCoO₂ full cells during precycling at 25 °C in the LCE, PWSE, and PWSE+LiFMDFB+AgNO₃.

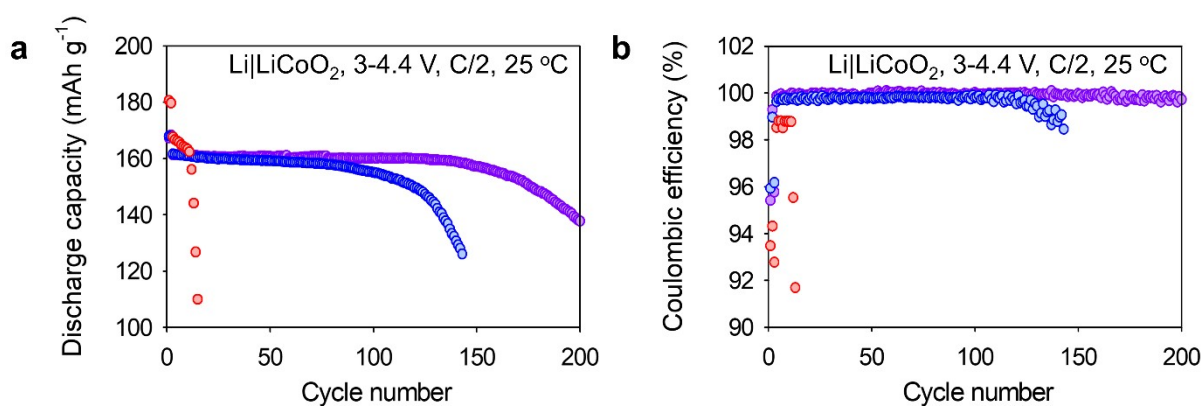


Fig. S36. Cycle performance of Li|LiCoO₂ full cells with a charge voltage cut-off of 4.4 V vs. Li/Li⁺ at 25 °C. Magnified (a) discharge capacity and (b) Coulombic efficiency (CE).

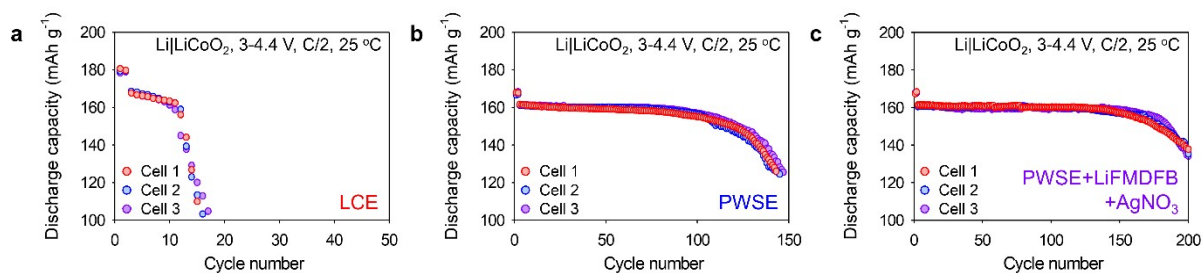


Fig. S37. Reproducibility of cycle performance of Li|LiCoO₂ full cells cycled with (a) LCE, (b) PWSE, and (c) PWSE+LiFMDFB+AgNO₃ electrolytes with a charge voltage cut-off of 4.4 V vs. Li/Li⁺ at 25 °C.

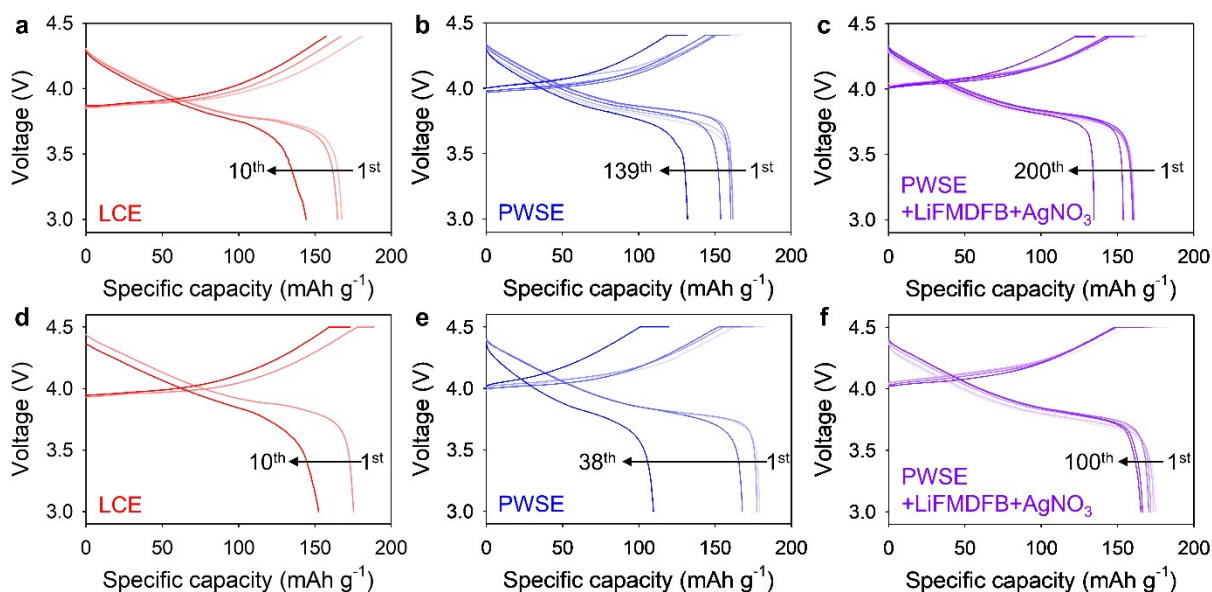


Fig. S38. Electrochemical performance of Li|LiCoO₂ full cells cycled in the LCE, PWSE, and PWSE+LiFMDFB+AgNO₃. Voltage profiles of Li|LiCoO₂ full cells with a charge cut-off voltage of 4.4 V vs. Li/Li⁺, cycled in the (a) LCE, (b) PWSE, and (c) PWSE+LiFMDFB+AgNO₃, and charge cut-off voltage of 4.5 V vs. Li/Li⁺, cycled in the (d) LCE, (e) PWSE, and (f) PWSE+LiFMDFB+AgNO₃.

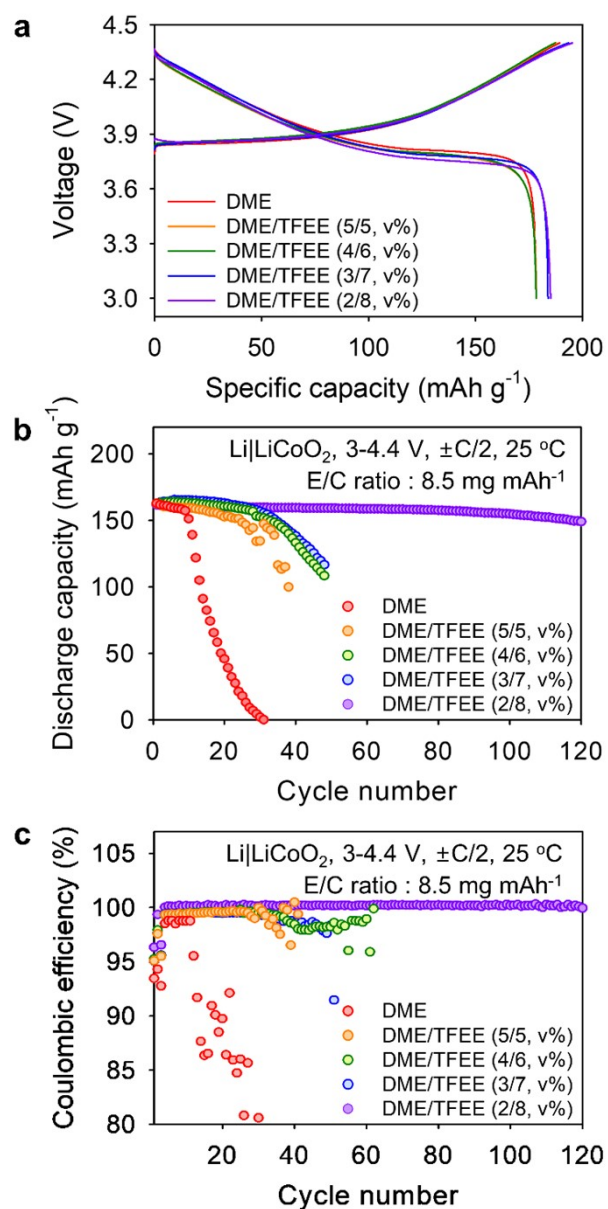


Fig. S39. Electrochemical characteristics of Li|LiCoO₂ full cells cycled in the DME, DME/TFEE (5/5, v%) (LiFSI DME/TFEE (1.3 M; 5/5, v%)), DME/TFEE (4/6, v%) (LiFSI DME/TFEE (1.3 M; 4/6, v%)), DME/TFEE (3/7, v%) (LiFSI DME/TFEE (1.3 M; 3/7, v%)), and DME/TFEE (2/8, v%) (LiFSI DME/TFEE (1.3 M; 2/8, v%)). (a) Voltage profiles during precycling and (b-c) cycle performance of Li|LiCoO₂ full cells in the potential range of 3.0 V to 4.4 V vs. Li/Li⁺ at 25 °C.

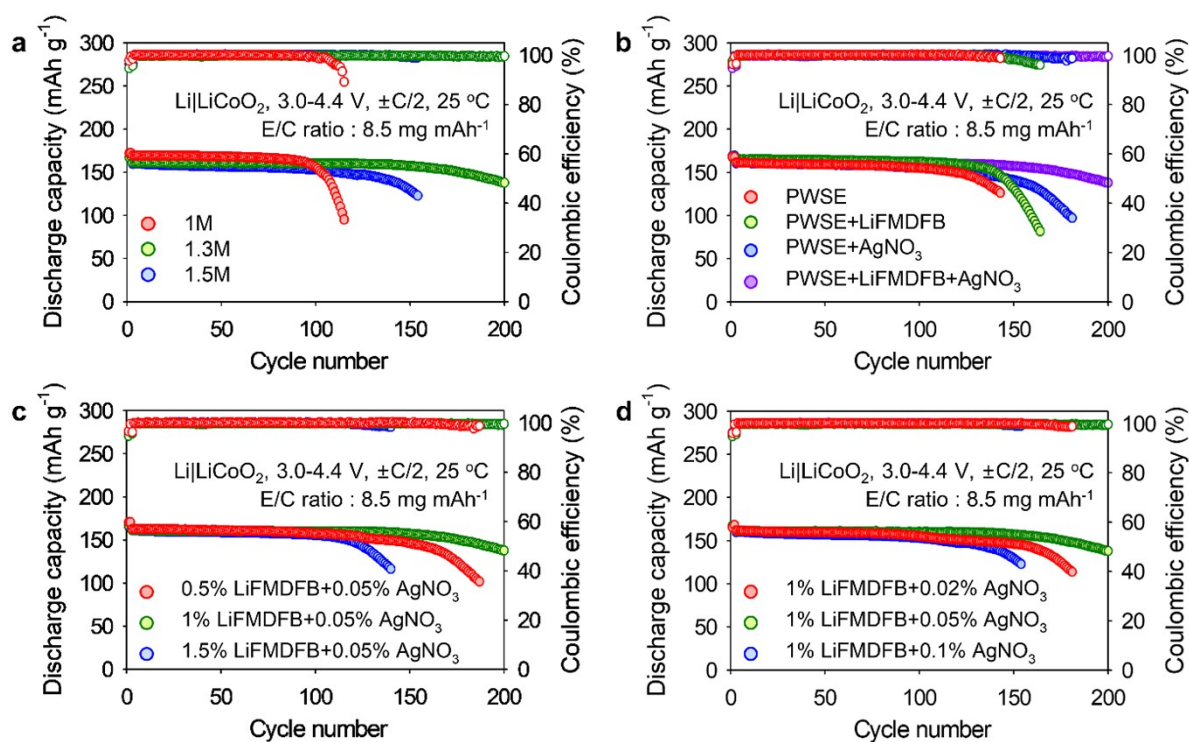


Fig. S40. Electrochemical characteristics of Li|LiCoO₂ full cells cycled with various salt and additive concentrations. (a) Cycle performance of Li|LiCoO₂ full cells cycled with LiFSI DME/TFEE (1 M; 2/8, v%)+1% LiFMDFB+0.05% AgNO₃ (1 M), LiFSI DME/TFEE (1.3 M; 2/8, v%)+1% LiFMDFB+0.05% AgNO₃ (1.3 M), and LiFSI DME/TFEE (1.5 M; 2/8, v%)+1% LiFMDFB+0.05% AgNO₃ (1.5 M) electrolytes. (b) Cycle performance of Li|LiCoO₂ full cells cycled with LiFSI DME/TFEE (1.3 M; 2/8, v%) (TFEE), LiFSI DME/TFEE (1.3 M; 2/8, v%)+1% LiFMDFB (PWSE+LiFMDFB), LiFSI DME/TFEE (1.3 M; 2/8, v%)+0.05% AgNO₃ (PWSE+AgNO₃), and LiFSI DME/TFEE (1.3 M; 2/8, v%)+1% LiFMDFB+0.05% AgNO₃ (PWSE+LiFMDFB+AgNO₃). (c) Cycle performance of Li|LiCoO₂ full cells cycled with LiFSI DME/TFEE (1.3 M; 2/8, v%)+0.5% LiFMDFB+0.05% AgNO₃ (0.5% LiFMDFB+0.05% AgNO₃), LiFSI DME/TFEE (1.3 M; 2/8, v%)+1% LiFMDFB+0.05% AgNO₃ (1% LiFMDFB+0.05% AgNO₃), and LiFSI DME/TFEE (1.3 M; 2/8, v%)+1.5% LiFMDFB+0.05% AgNO₃ (1.5% LiFMDFB+0.05% AgNO₃). (d) Cycle performance of Li|LiCoO₂ full cells cycled with LiFSI DME/TFEE (1.3 M; 2/8, v%)+1% LiFMDFB+0.02% AgNO₃ (1%

LiFMDFB+0.02% AgNO₃), LiFSI DME/TFEE (1.3 M; 2/8, v%)+1% LiFMDFB+0.05% AgNO₃ (1% LiFMDFB+0.05% AgNO₃), and LiFSI DME/TFEE (1.3 M; 2/8, v%)+1% LiFMDFB+0.1% AgNO₃ (1% LiFMDFB+0.1% AgNO₃) electrolytes. The aforementioned cells were cycled from 3.0 V to 4.4 V vs. Li/Li⁺ at 25 °C and C/2.

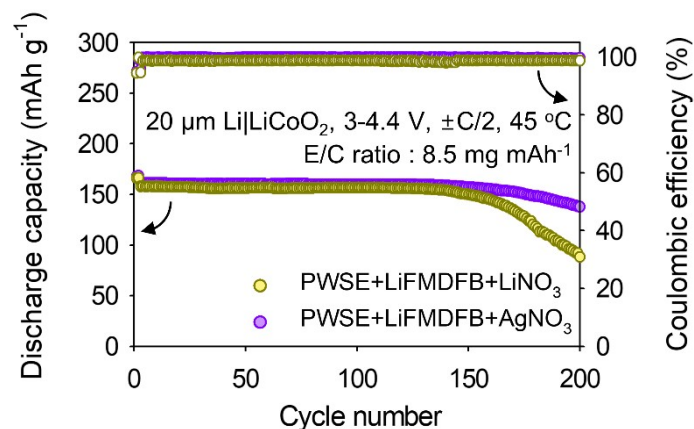


Fig. S41. Cycle performance of Li|LiCoO₂ full cells cycled with PWSE+LiFMDFB+LiNO₃ and PWSE+LiFMDFB+AgNO₃ electrolytes with a charge voltage cut-off of 4.4 V vs. Li/Li⁺ at 25 °C.

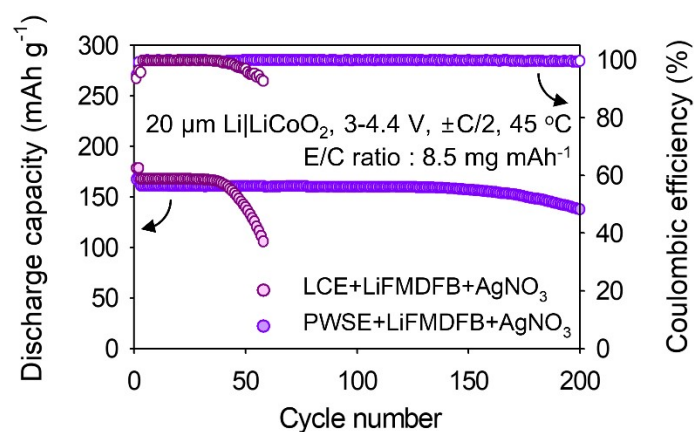


Fig. S42. Cycle performance of Li|LiCoO₂ full cells cycled with LCE+LiFMDFB+AgNO₃ and PWSE+LiFMDFB+AgNO₃ electrolytes with a charge voltage cut-off of 4.4 V vs. Li/Li⁺ at 25 °C.

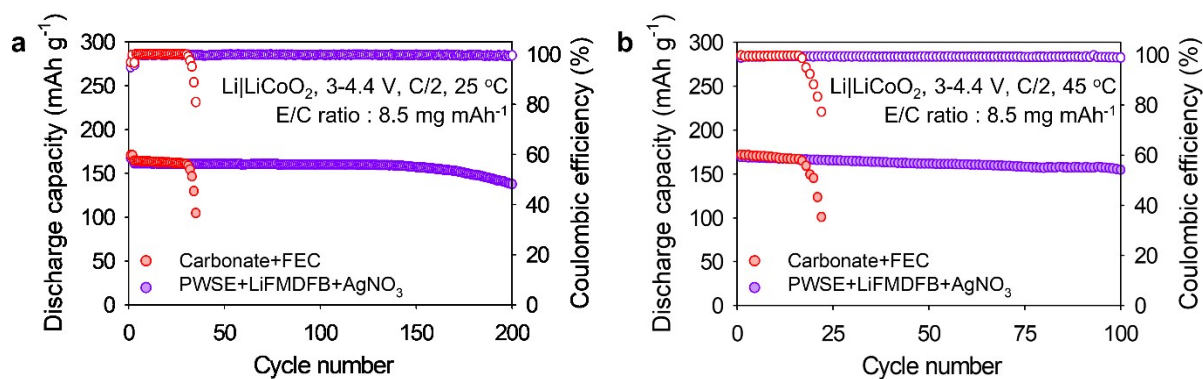


Fig. S43. Electrochemical characteristics of Li|LiCoO₂ full cells cycled with a carbonate-based electrolyte (LiPF₆ EC/DMC (1.3 M; 3/7, v%)+10% FEC, labeled Carbonate+FEC) and PWSE+LiFMDFB+AgNO₃. Cycle performance of Li|LiCoO₂ full cells from 3.0 V to 4.4 V vs. Li/Li⁺ at (a) 25 °C and (b) 45 °C.

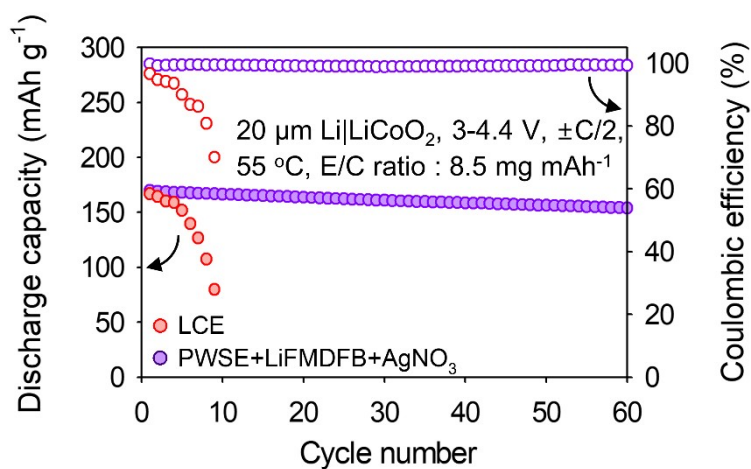


Fig. S44. Cyclability of Li|LiCoO₂ full cells with a charge cut-off voltage of 4.4 V vs. Li/Li⁺ at 55 °C.

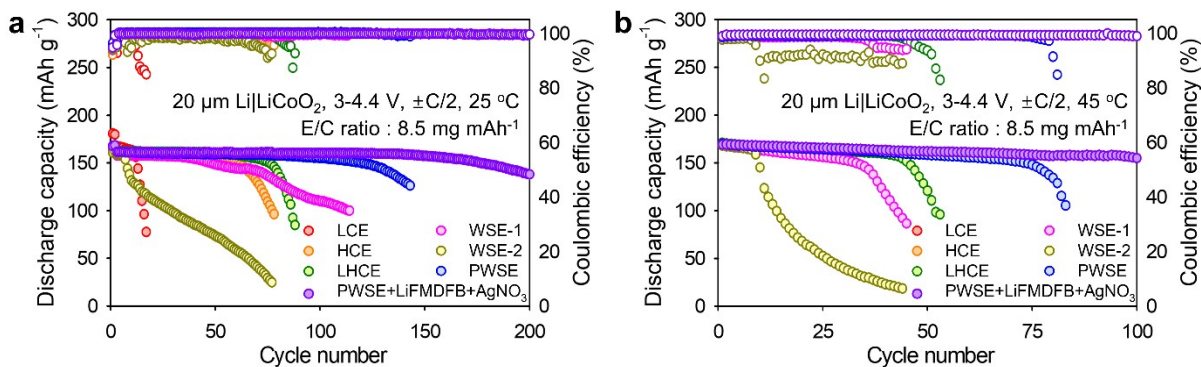


Fig. S45. Electrochemical characteristics of Li|LiCoO₂ full cells cycled in the LCE, HCE, LHCE, WSE-1, WSE-2, PWSE, and PWSE+LiFMDFB+AgNO₃. LiFSI DME (1.3 M) is labeled LCE, LiFSI DME (4 M) is labeled HCE, LiFSI DME/TTE (1.3 M; 2/8, v%) is labeled LHCE, LiFSI DEE (4 M) is labeled WSE-1, LiFSI DMP (2 M) is labeled WSE-2, LiFSI DME/TFEE (1.3 M; 2/8, v%) is labeled PWSE, and LiFSI DME/TFEE (1.3 M; 2/8, v%)+1% LiFMDFB+0.05% AgNO₃ is labeled PWSE+LiFMDFB+AgNO₃. Cycle performance of the aforementioned Li|LiCoO₂ full cells was analyzed from 3.0 V to 4.4 V vs. Li/Li⁺ at (a) 25 °C and (b) 45 °C.

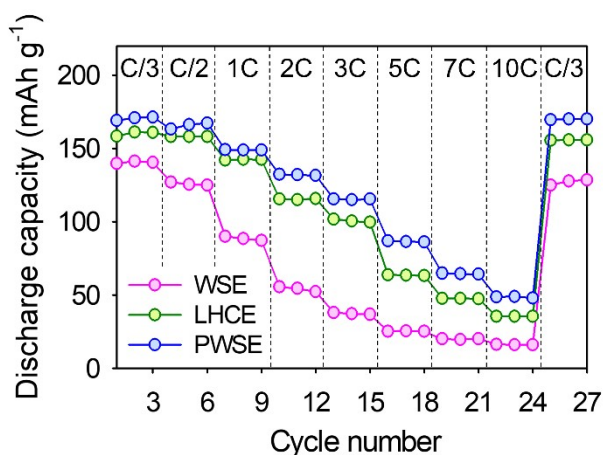


Fig. S46. Fast-charging performance of WSE, LHCE, and PWSE in Li|LiCoO₂ full cells. Discharge C-rate was fixed at C/3. 4 M LiFSI DEE is labeled as WSE, 1.3 M LiFSI DME/TTE (2/8, v%) is labeled as LHCE, and 1.3 M LiFSI DME/TFEE (2/8, v%) is labeled as PWSE.

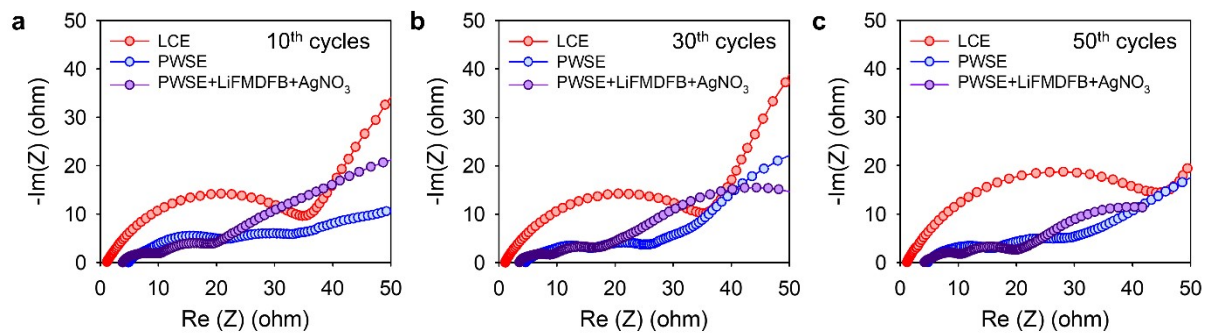


Fig. S47. Electrochemical impedance spectra of Li|LiCoO₂ full cells in the LCE, PWSE, and PWSE+LiFMDFB+AgNO₃ after the (a) 10th, (b) 30th, and (c) 50th cycles.

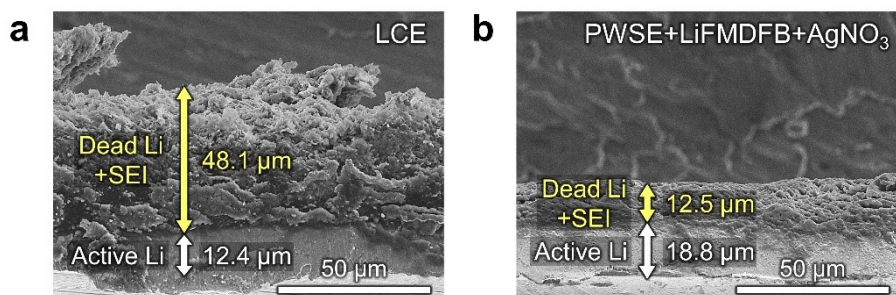


Fig. S48. Cross-sectional SEM images of lithium-metal anodes cycled with the (a) LCE and (b) PWSE+LiFMDFB+AgNO₃ in Li|LiCoO₂ full cells after 30 cycles at C/2 and 45 °C.

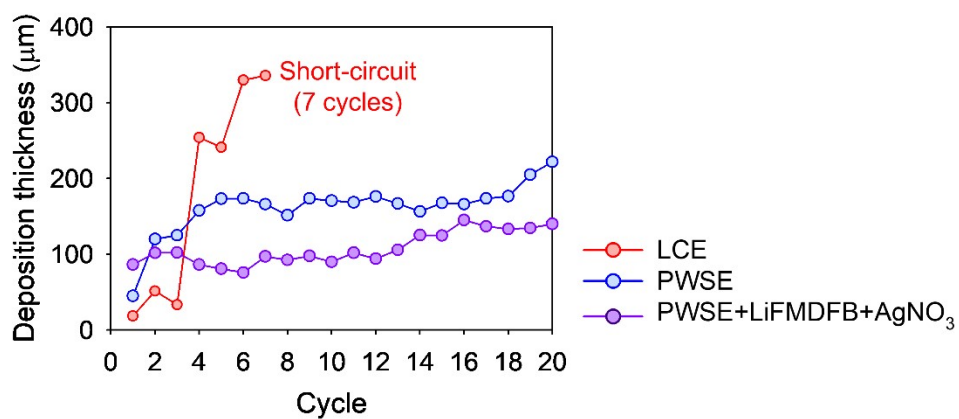


Fig. S49. Li deposition thickness on cycling Li|Li cells with the LCE, PWSE, and PWSE+LiFMDFB+AgNO₃ (during in-situ OM analysis).

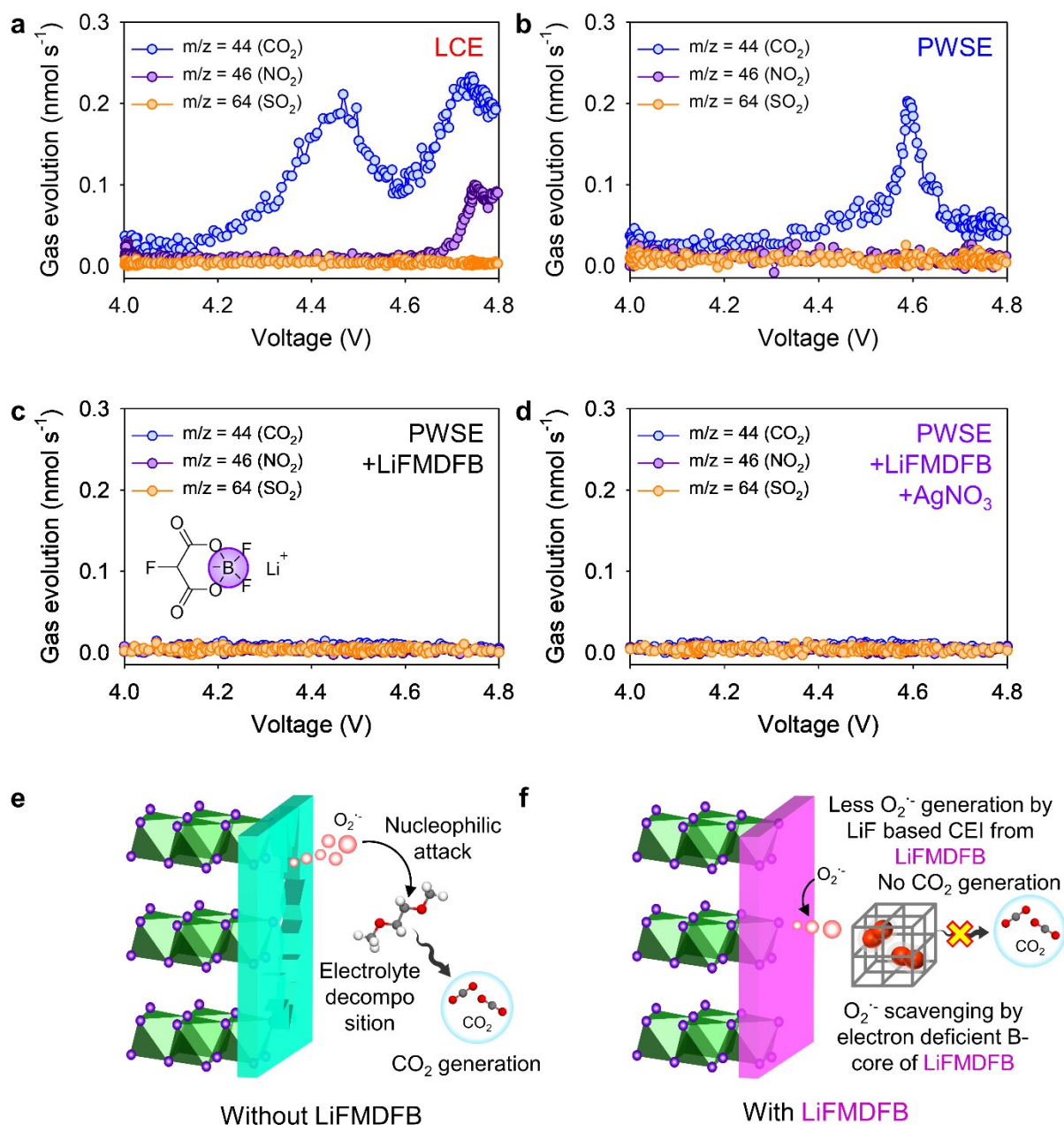


Fig. S50. In-situ differential electrochemical mass spectrometry (DEMS) analysis showing CO₂ (m/z = 44), NO₂ (m/z = 46), and SO₂ (m/z = 64) evolution with the (a) LCE, (b) PWSE, (c) PWSE+LiFMDFB, and (d) PWSE+LiFMDFB+AgNO₃ during the first charging of the Li|LiCoO₂ full cell from the open circuit voltage (OCV) to 4.8 V vs. Li/Li⁺. Schematic illustration of gas evolution or scavenging (e) with and (f) without LiFMDFB.

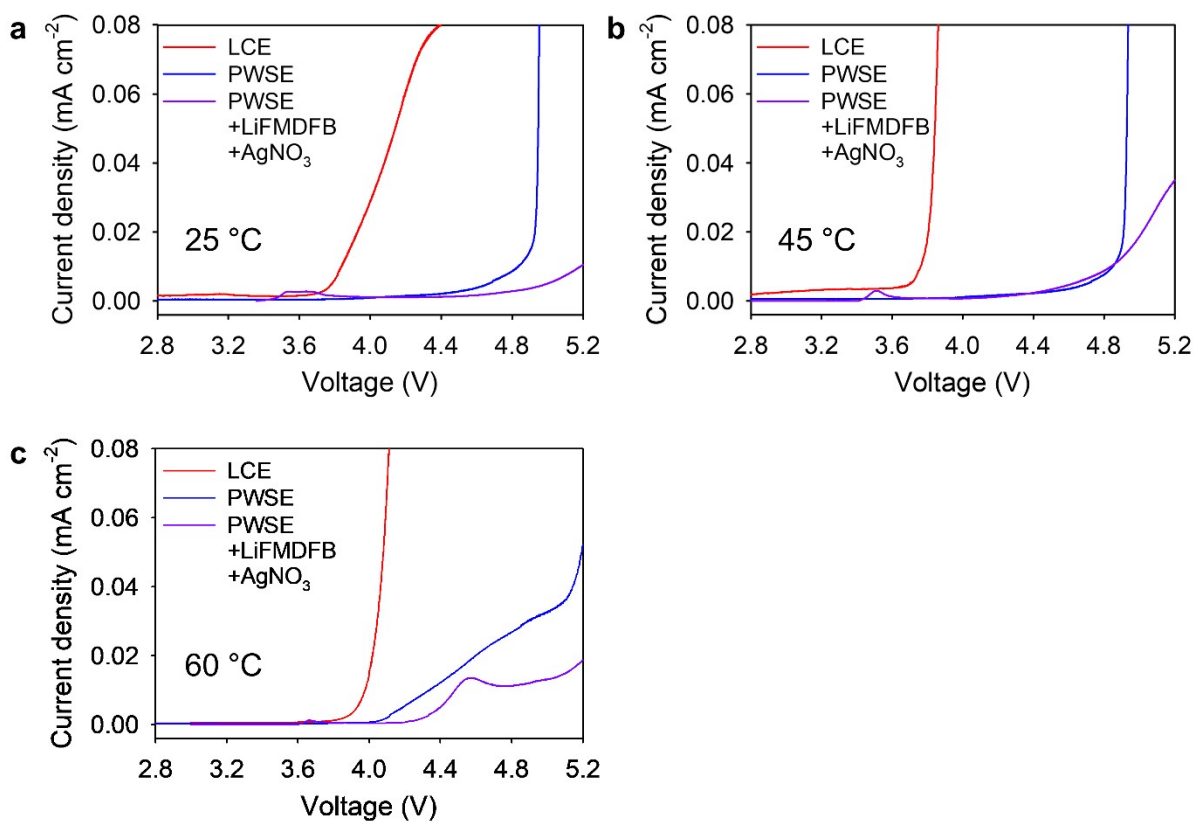


Fig. S51. Anodic stability of electrolytes with a stainless-steel working electrode. Linear sweep voltammetry (LSV) measurements were conducted from the OCV to 5.2 V vs. Li/Li⁺ at a scan rate of 1 mV s⁻¹ at (a) 25 °C, (b) 45 °C, and (c) 60 °C.

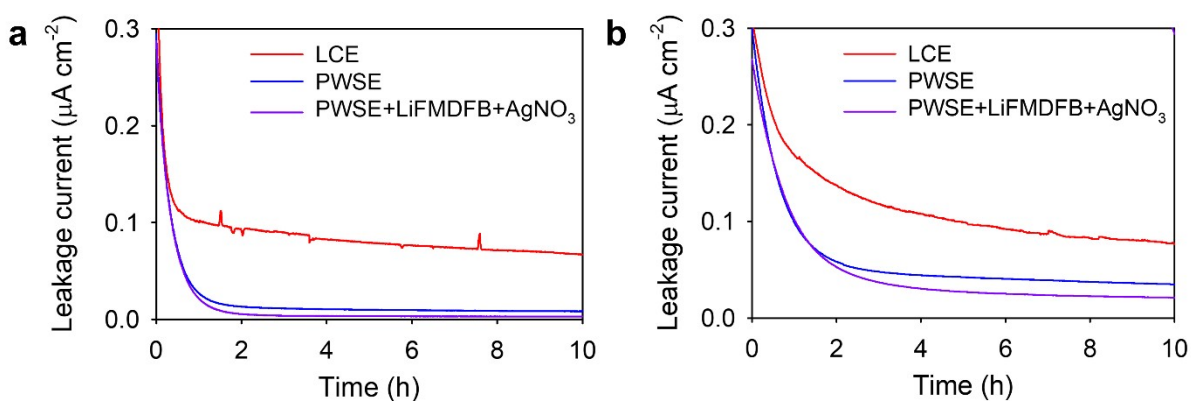


Fig. S52. Electrochemical floating test of Li|LiCoO₂ full cells at (a) 4.4 V vs. Li/Li⁺ and (b) 4.6 V vs. Li/Li⁺, 10 h after precycling at 25 °C.

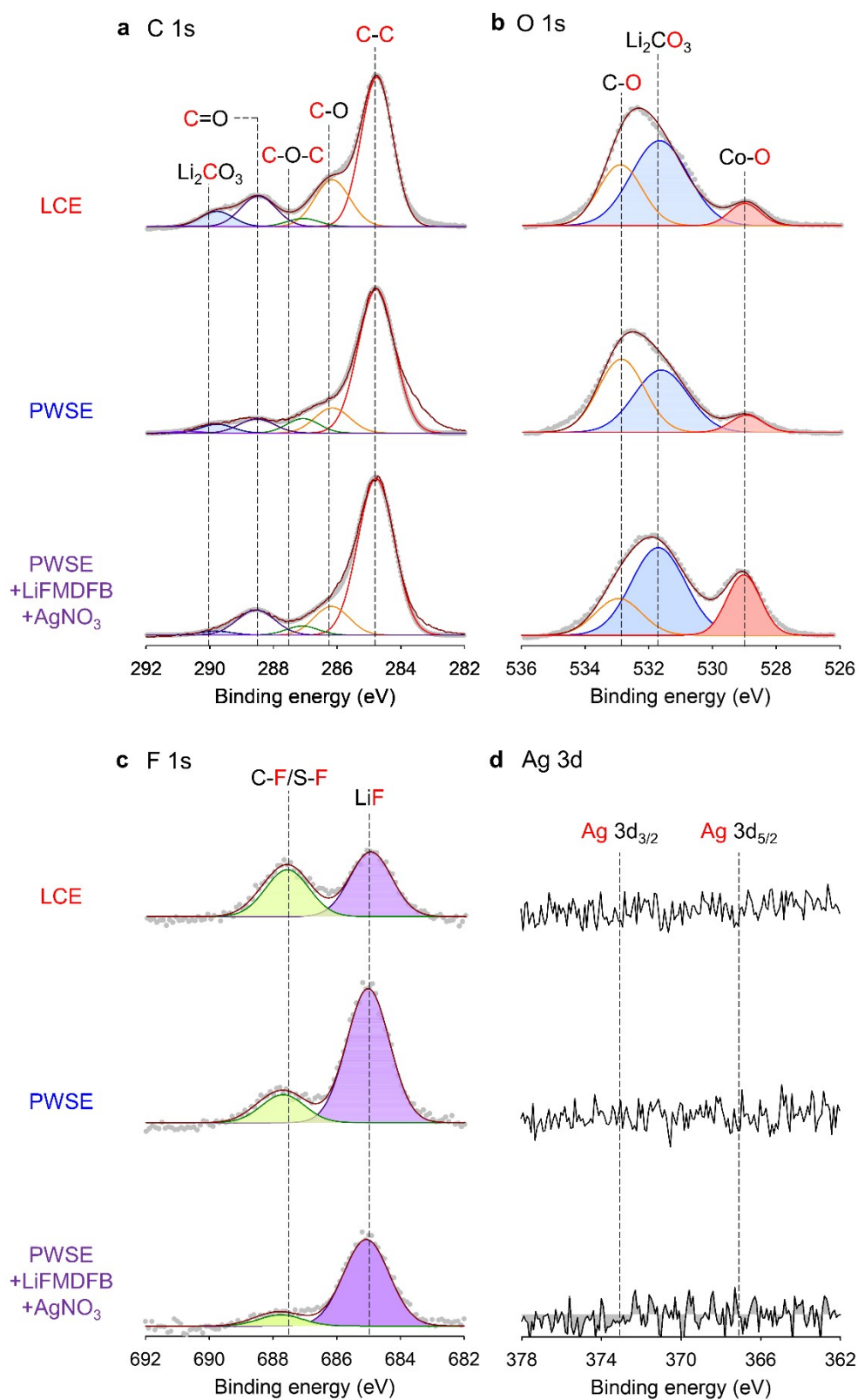


Fig. S53. Surface chemistry of LiCoO₂ cathodes retrieved from Li|LiCoO₂ full cells cycled with the LCE, PWSE, and PWSE+LiFMDFB+AgNO₃. (a) C 1s, (b) O 1s, (c) F 1s, and (d) Ag 3d XPS profiles of LiCoO₂ cathodes after precycling at 25 °C.

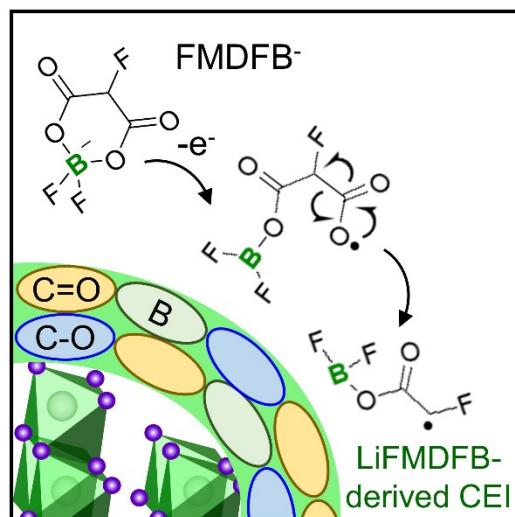


Fig. S54. Schematic illustration of LiFMDFB-derived CEI on the LiCoO₂ cathode.

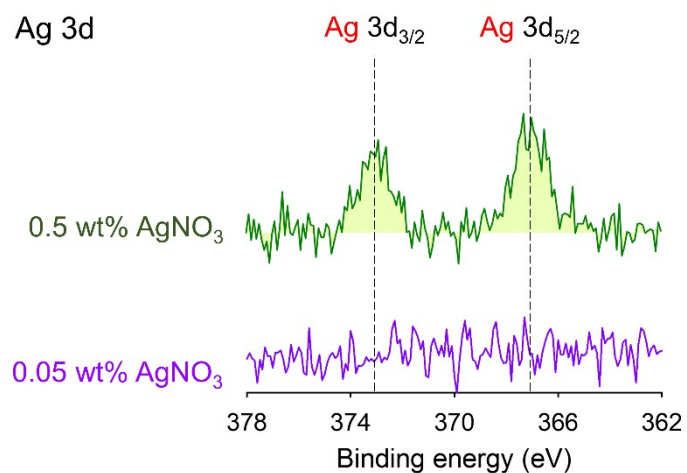


Fig. S55. Surface chemistry of LiCoO₂ cathodes retrieved from Li|LiCoO₂ full cells precycled with the 0.05 wt% AgNO₃ (1.3 M LiFSI DME/TFEE (2/8, v%)+1% LiFMDFB+0.05% AgNO₃) and 0.5 wt% AgNO₃ (1.3 M LiFSI DME/TFEE (2/8, v%)+1% LiFMDFB+0.5% AgNO₃) electrolytes. Ag 3d XPS profiles of LiCoO₂ cathodes after precycling at 25 °C.

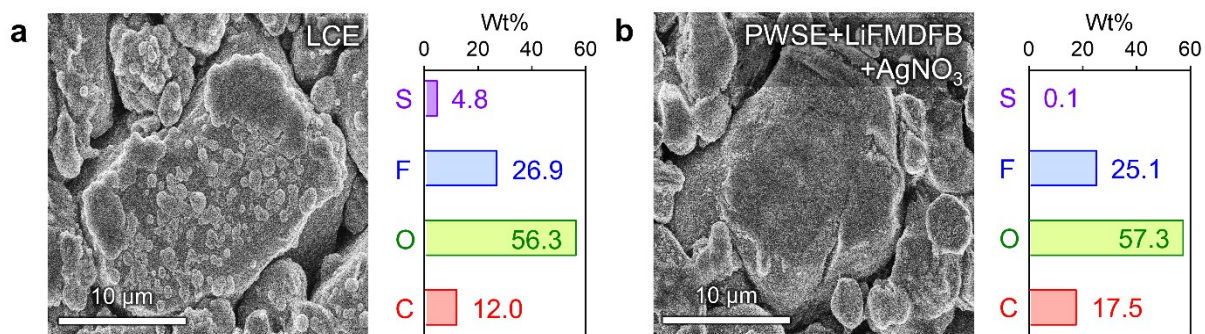


Fig. S56. SEM images and EDAX of LiCoO₂ cathodes cycled with the (a) LCE and (b) PWSE+LiFMDFB+AgNO₃ after 30 cycles at C/2 and 45 °C.

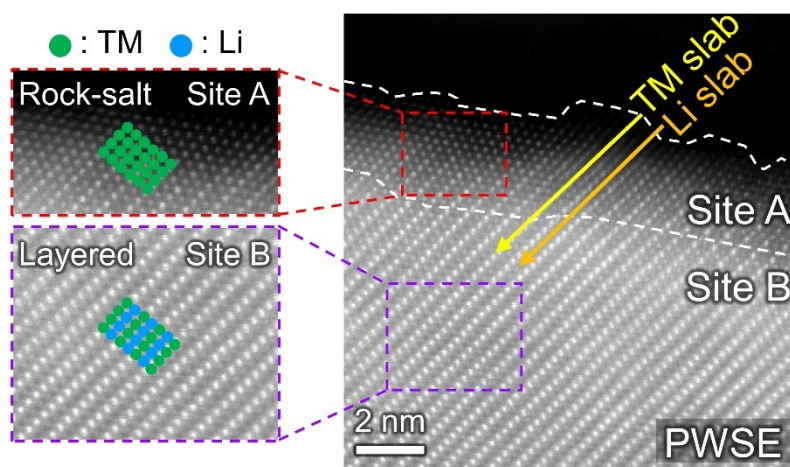


Fig. S57. STEM images of LiCoO₂ cathodes cycled with PWSE.

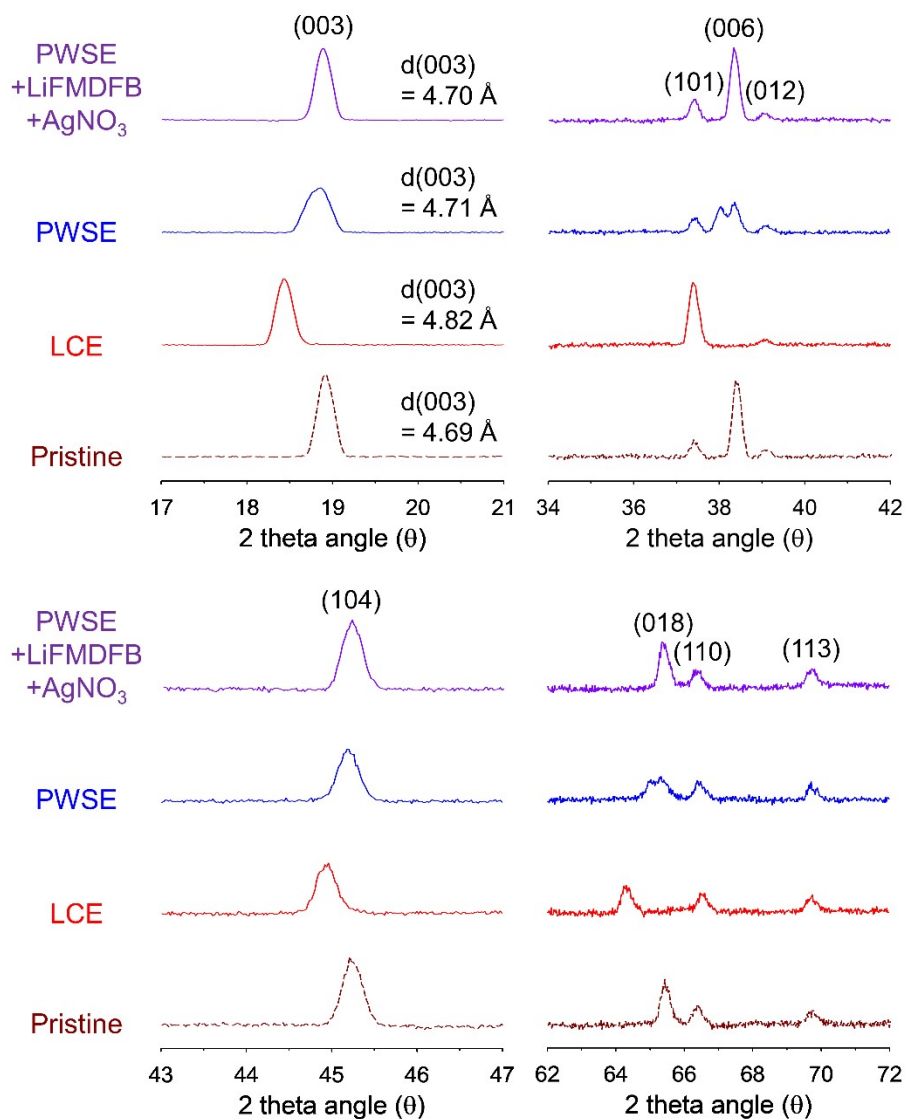


Fig. S58. X-ray diffraction patterns (XRD) of a pristine LiCoO_2 cathode and LiCoO_2 cathodes retrieved from $\text{Li}|\text{LiCoO}_2$ full cells after 100th cycles with the LCE, PWSE, and PWSE+LiFMDFB+ AgNO_3 electrolytes at C/2 and 25 °C.

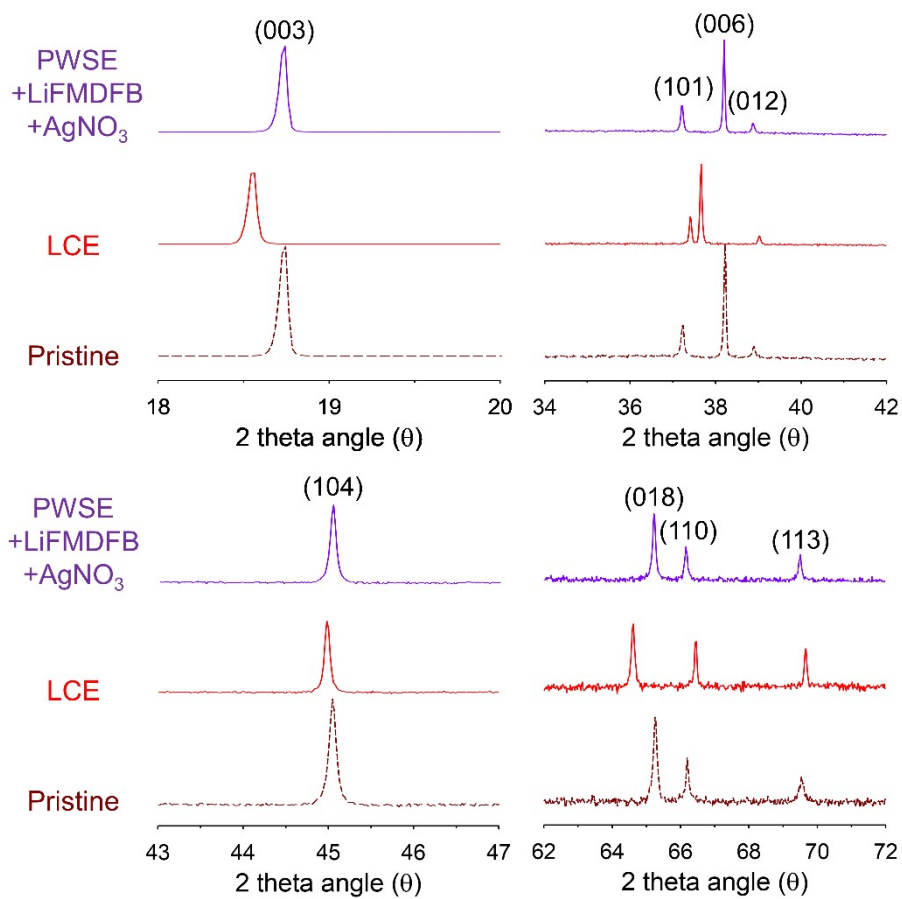


Fig. S59. XRD patterns of a pristine LiCoO_2 cathode and LiCoO_2 cathodes retrieved from $\text{Li}|\text{LiCoO}_2$ full cells after 30 cycles with the LCE and PWSE+LiFMDFB+ AgNO_3 electrolytes at C/2 and 45 °C.

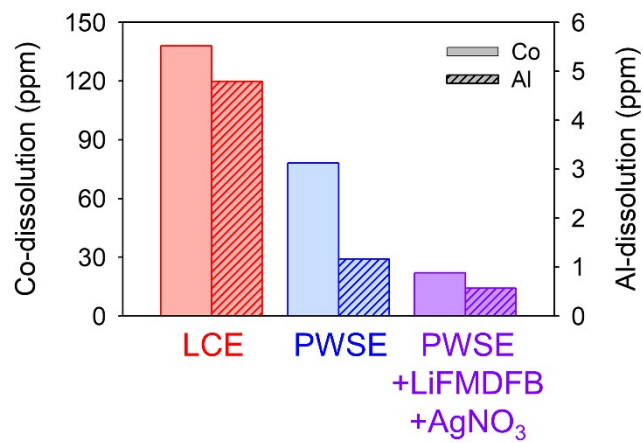


Fig. S60. Concentration of Co- and Al-dissolved in the electrolytes after being kept in contact with a fully delithiated LiCoO_2 cathode for 7 days at 60°C .

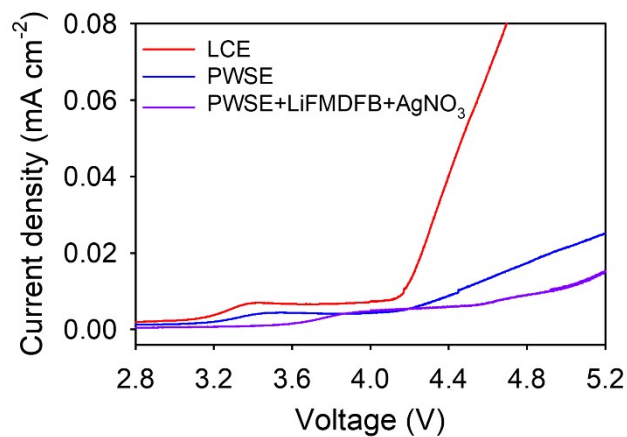


Fig. S61. Anodic stability of electrolytes with an Al working electrode. LSV measurements were conducted from the OCV to 5.2 V vs. Li/Li⁺ at a scan rate of 1 mV s⁻¹ at 25 °C.

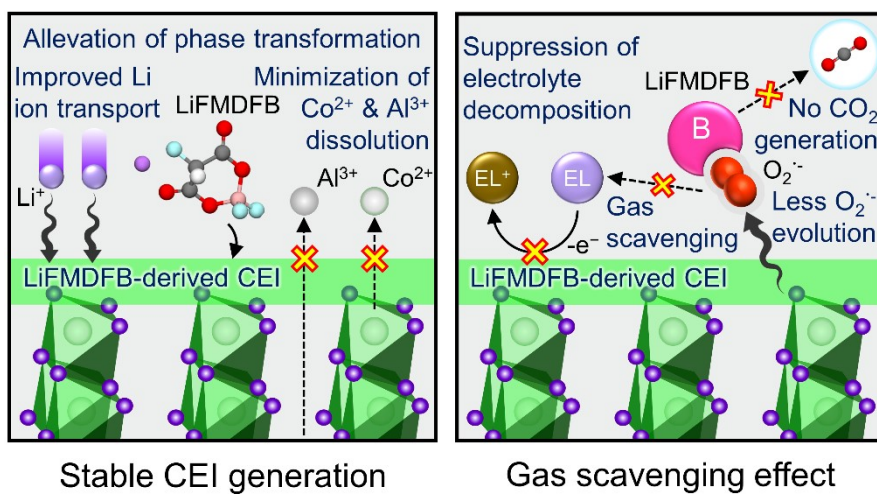


Fig. S62. Influence of the LiFMDFB-derived CEI on the LiCoO₂ cathode.

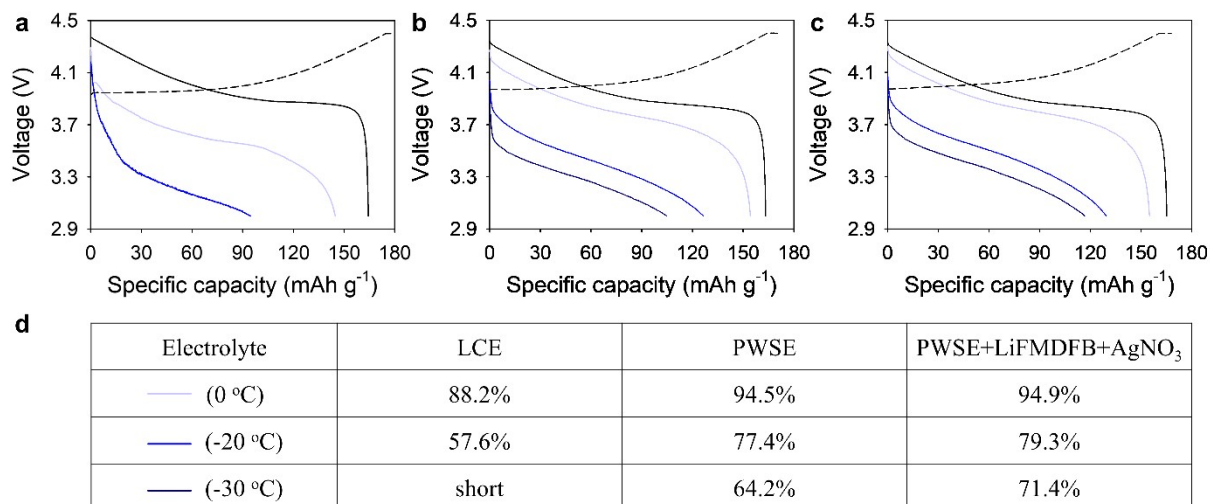


Fig. S63. Electrochemical performance of Li|LiCoO₂ full cells at low temperatures. Capacity retention of Li|LiCoO₂ full cells with the (a) LCE, (b) PWSE, and (c) PWSE+LiFMDFB+AgNO₃ at 0 °C, -20 °C, and -30 °C. (d) Capacity retention of each electrolyte at 0 °C, -20 °C, and -30 °C. Discharging was conducted at C/5 from the fully charged state (SOC 100% at 25 °C).

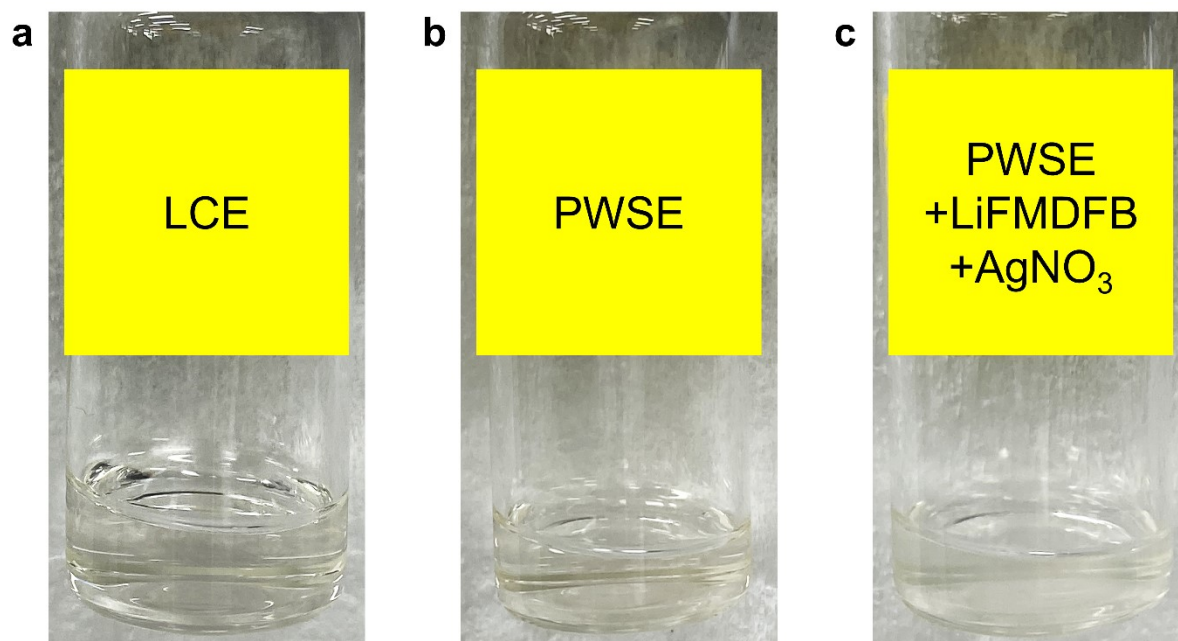


Fig. S64. Images of (a) LCE, (b) PWSE, and (c) PWSE+LiFMDFB+AgNO₃ electrolytes after storage at -20 °C for 1 week.

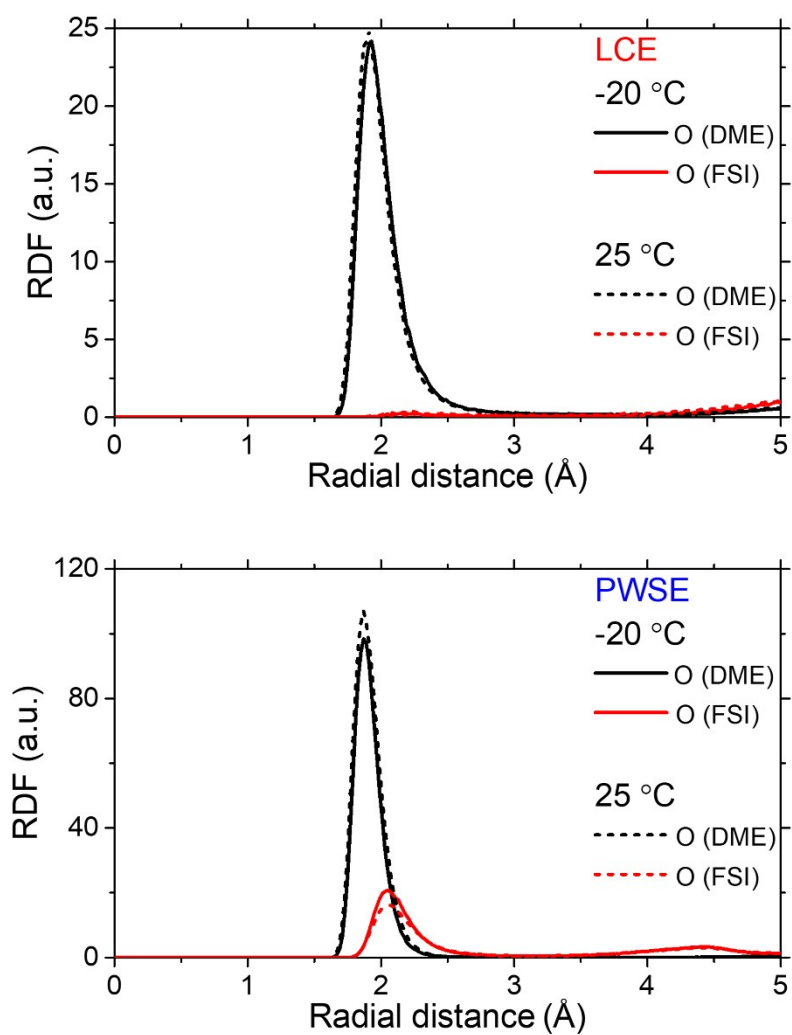


Fig. S65. RDF results of DME (oxygen atoms) and FSI anion (oxygen atoms) with respect to Li^+ -ions according to the temperature (i.e., $-20\text{ }^\circ\text{C}$ and $25\text{ }^\circ\text{C}$) in LCE and PWSE conditions.

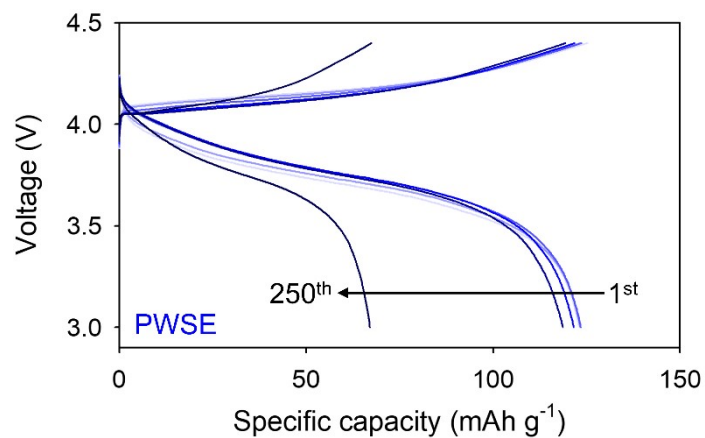


Fig. S66. Voltage profiles of Li|LiCoO₂ full cells with a charge cut-off voltage of 4.4 V vs. Li/Li⁺ at -20 °C, cycled in the PWSE.

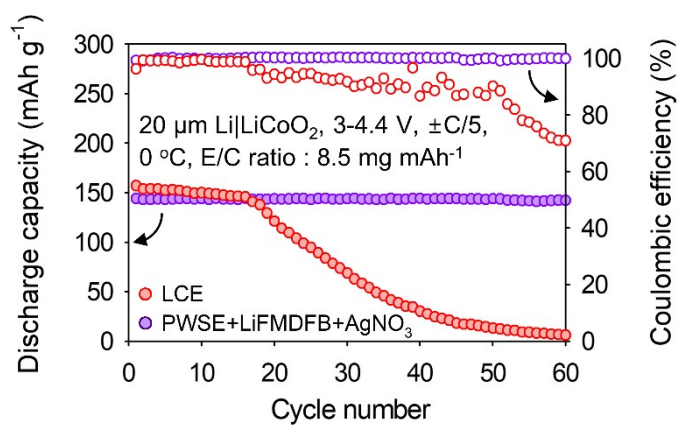


Fig. S67. Cyclability of Li|LiCoO₂ full cells with a charge cut-off voltage of 4.4 V vs. Li/Li⁺ at 0 °C.

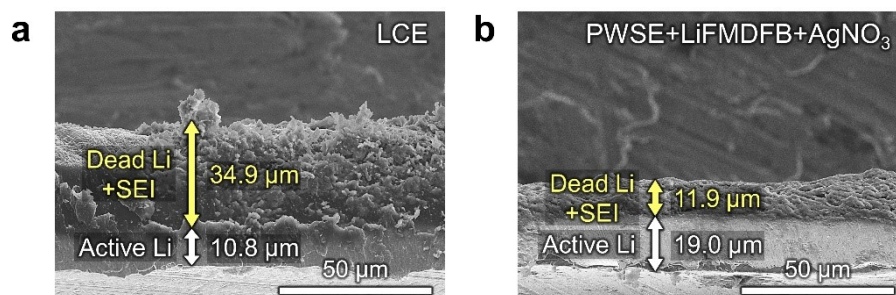


Fig. S68. Cross-sectional SEM images of lithium-metal anodes cycled with (a) LCE and (b) PWSE+LiFMDFB+AgNO₃ in Li|LiCoO₂ full cells after 30 cycles at C/5 and -20 °C.

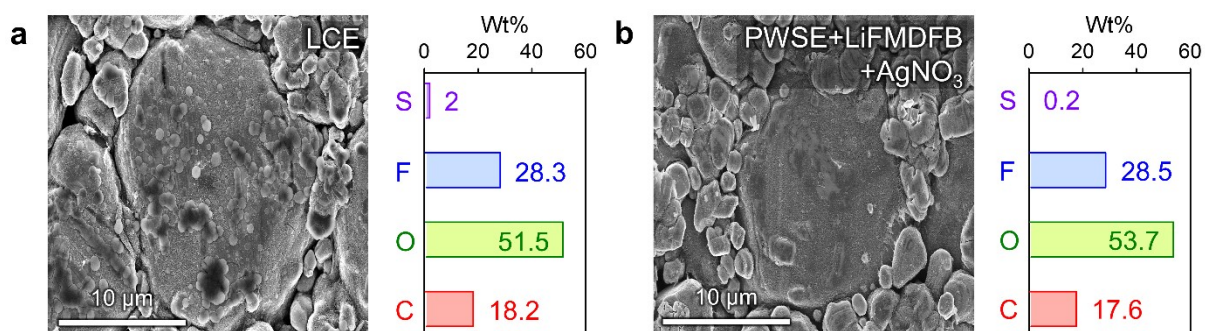


Fig. S69. SEM images and EDAX of LiCoO₂ cathodes cycled with the (a) LCE and (b) PWSE+LiFMDFB+AgNO₃ after 30 cycles at C/5 and -20 °C.

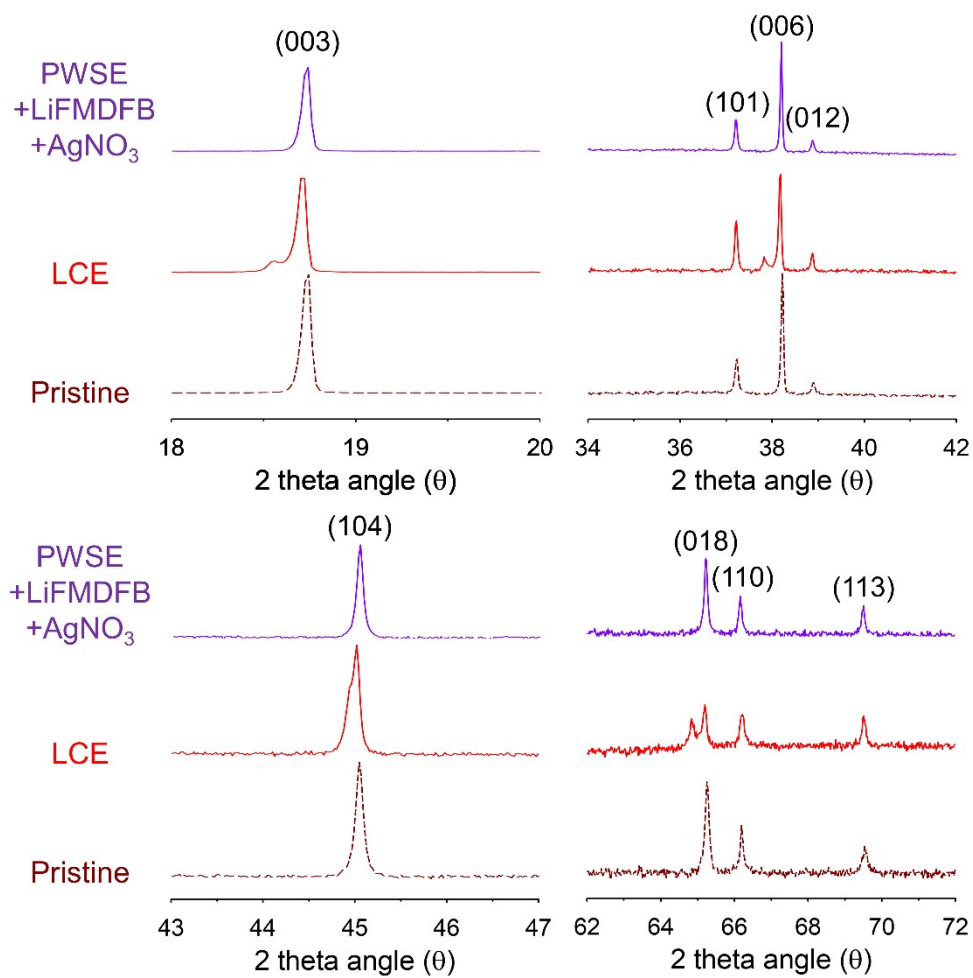


Fig. S70. XRD patterns of a pristine LiCoO_2 cathode and LiCoO_2 cathodes retrieved from $\text{Li}|\text{LiCoO}_2$ full cells after 30th cycles with the LCE and PWSE+LiFMDFB+ AgNO_3 electrolytes at C/5 and -20°C .

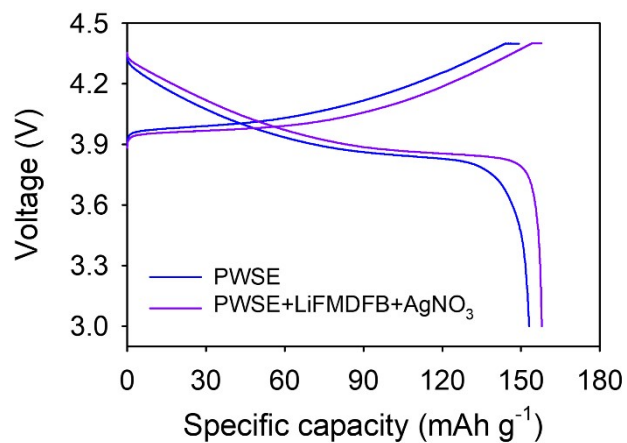


Fig. S71. Recovery test of Li|LiCoO₂ full cells with the PWSE and PWSE+LiFMDFB+AgNO₃ at 25 °C.

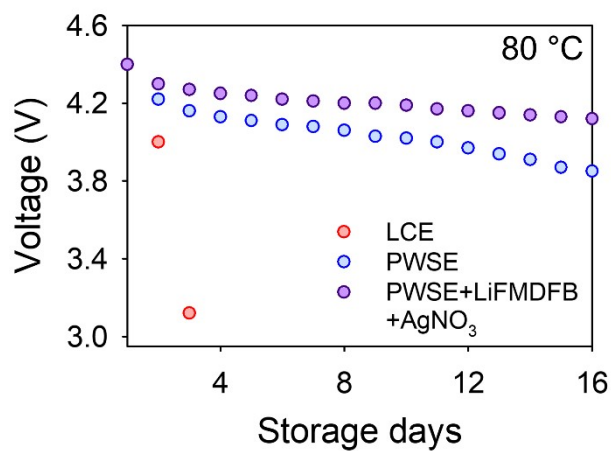


Fig. S72. Li|LiCoO₂ full cell storage test (checking the OCV drop from an SOC of 100%) at 80 °C.

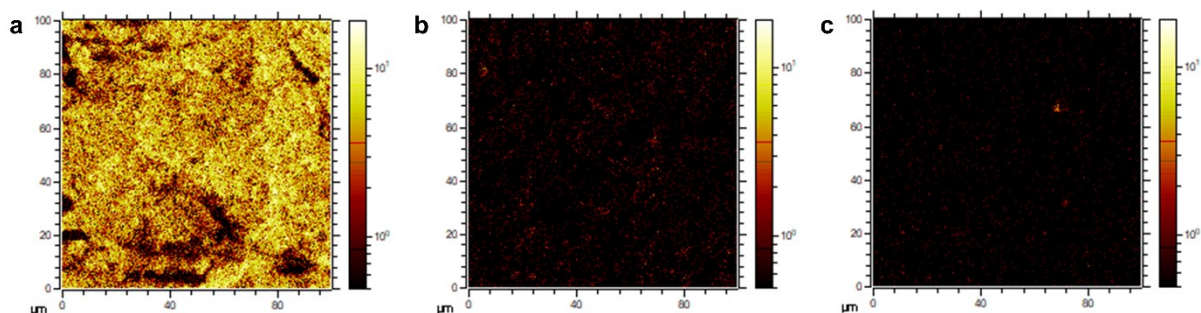


Fig. S73. TOF-SIMS CoF₂⁺-ion maps of Li metal anodes in the fully delithiated state in Li|LiCoO₂ full cells with the (a) LCE, (b) PWSE, and (c) PWSE+LiFMDFB+AgNO₃, after 10 days of storage at 60 °C.

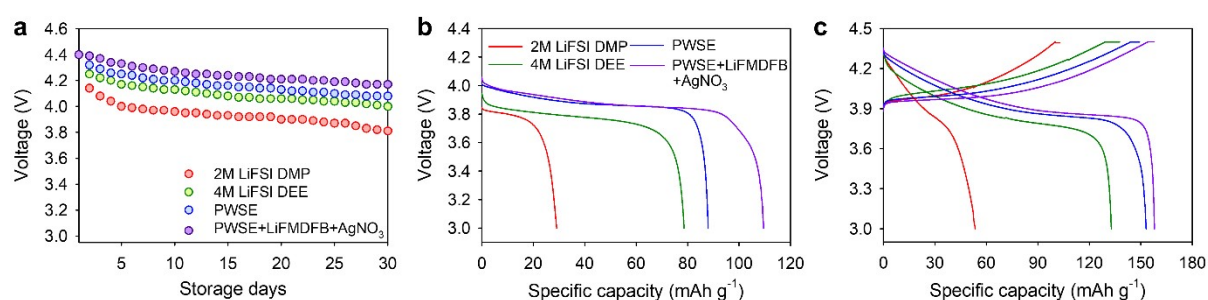
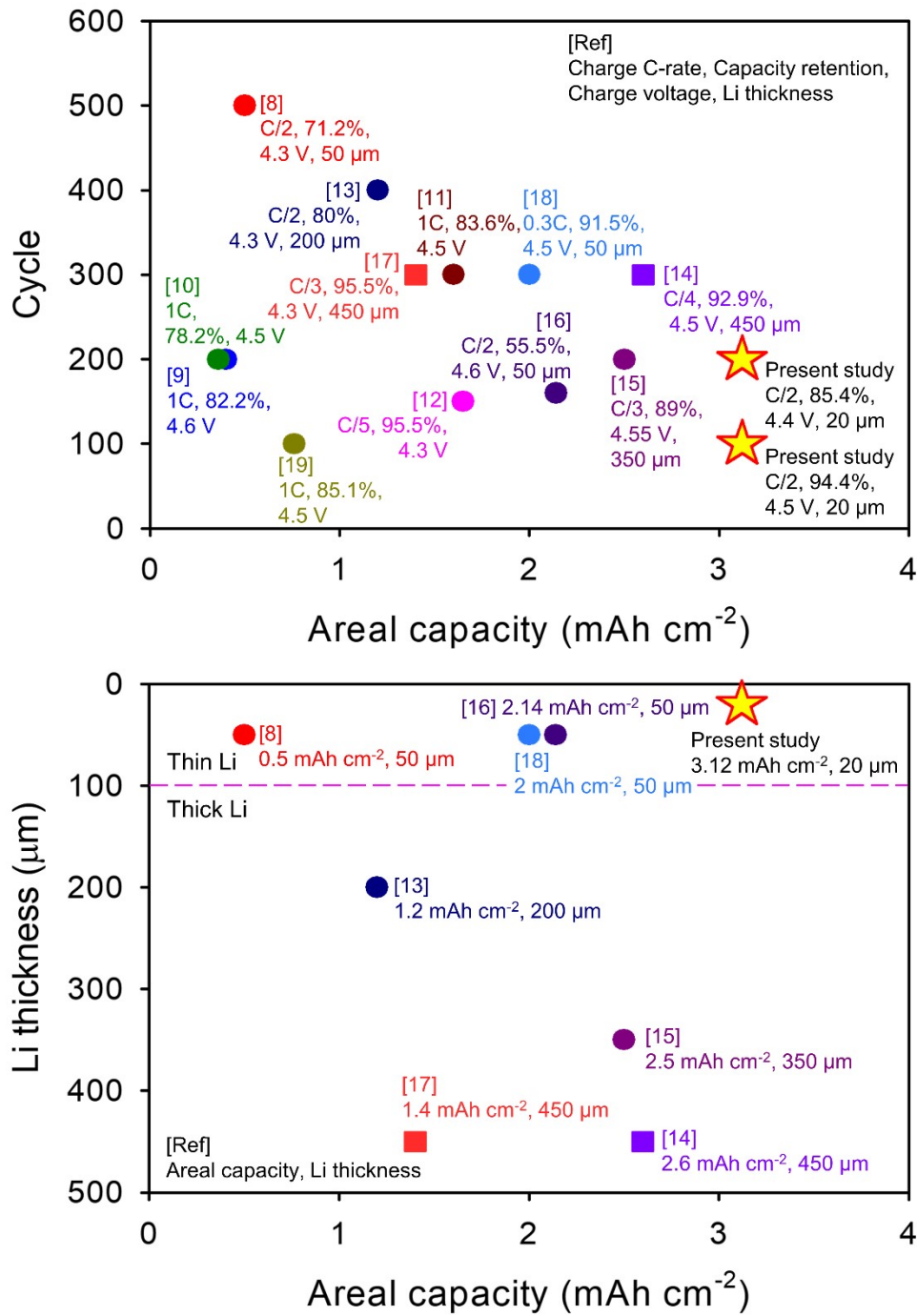


Fig. S74. (a) Li|LiCoO₂ full cell storage test at 60 °C for 30 days, analyzing the OCV drop from a 100% state of charge. (b) Capacity retention of Li|LiCoO₂ full cells at 25 °C after 30 days storage at 60 °C. After the storage test at 60 °C, the full cells are discharged up to 3 V vs. Li/Li⁺ at C/10. (c) Recovery test of Li|LiCoO₂ full cells at 25 °C.



	Reference	Electrolyte	Operating voltage (V)	Current density (mA cm ⁻²)	Areal capacity (mAh cm ⁻²)	Li thickness (μm, utilization)	Cycle retention (@ cycle, temperature)
★	Present study	1.3M LiFSI DME/TFEE (2/8, v%) +1% LiFMDFB +0.05% AgNO ₃	3.0-4.4	±1.56	3.12	20	85.4 (@200, 25 °C)
			3.0-4.5				72.1 (@300, -20 °C)
							94.4 (@100, 25 °C)

●	[8]	(0.3M LiDFOB + 0.2M LiBF ₄) DEC/FEC/FB (3.5/1.5/5, v%)	3.0-4.3	±0.25	0.5	50	71.2 (@500, -20 °C)
●	[9]	1M LiPF ₆ EC/DEC (3/7, v%)+0.5% TPCB	3.0-4.6	±0.4	0.4	Not provided	82.2 (@200, 30 °C)
●	[10]	1M LiPF ₆ EC/EMC/DEC/DMC (1/1/1, v%)+2% TCEB	2.75-4.5	±0.36	0.36	Not provided	78.2 (@200, 25 °C)
●	[11]	1.2M LiPF ₆ FEC/DMC/HFE (1/1/1, v%)+0.15M LiDFOB	2.75-4.5	±1.6	1.6	Not provided	83.6 (@300, 25 °C)
●	[12]	1M LiFPA EC/DMC	3.0-4.3	±0.33	1.65	Not provided	95.5 (@150, 25 °C)
●	[13]	LiTFSI/P13FSI/TTE (1/2/2, mol%)	3.0-4.3	±0.6	1.2	200	80.0 (@400, 25 °C)
■	[14]	LiFSI/DME/TTE (1/1/3, mol%)	3.0-4.5	+0.63, -1.9	2.6	450	92.9 (@300, 25 °C)
●	[15]	1m LiFSI DMCF ₃ SA	3.0-4.55	+0.75, -2.5	2.5	350	89.0 (@200, 25 °C)
●	[16]	1.5M LiBF ₄ DME/FEC (1/1, v%)	3.0-4.6	+1.07, -2.14	2.14	50	55.5 (@160, 25 °C)
■	[17]	(1M LiTFSI+200 mM LiNO ₃) DME	3.0-4.3	±0.47	1.4	450	95.5 (@300, 25 °C)
●	[18]	1M LiDFOB DME/THE (1/1, v%)	3.0-4.5	±0.6	2	50	91.5 (@300, 25 °C)
				±0.4			86.0 (@50, -20 °C)
●	[19]	1M LiPF ₆ EC/DEC (1/1, wt%)+0.3% TAEC	3.0-4.5	±0.76	0.76	Not provided	85.1 (@100, 25 °C)

Fig. S75. Comparison of the cycle performance, operating voltage, current density, areal capacity, and Li metal thickness of Li|LiCoO₂ full cells. Square dots indicate electrolytes containing ether-based solvents, while circle dots indicate the other electrolyte (excluding ether-based electrolytes). The cycle performance and capacity retention of the LiCoO₂ full cells investigated in this study are marked with stars.

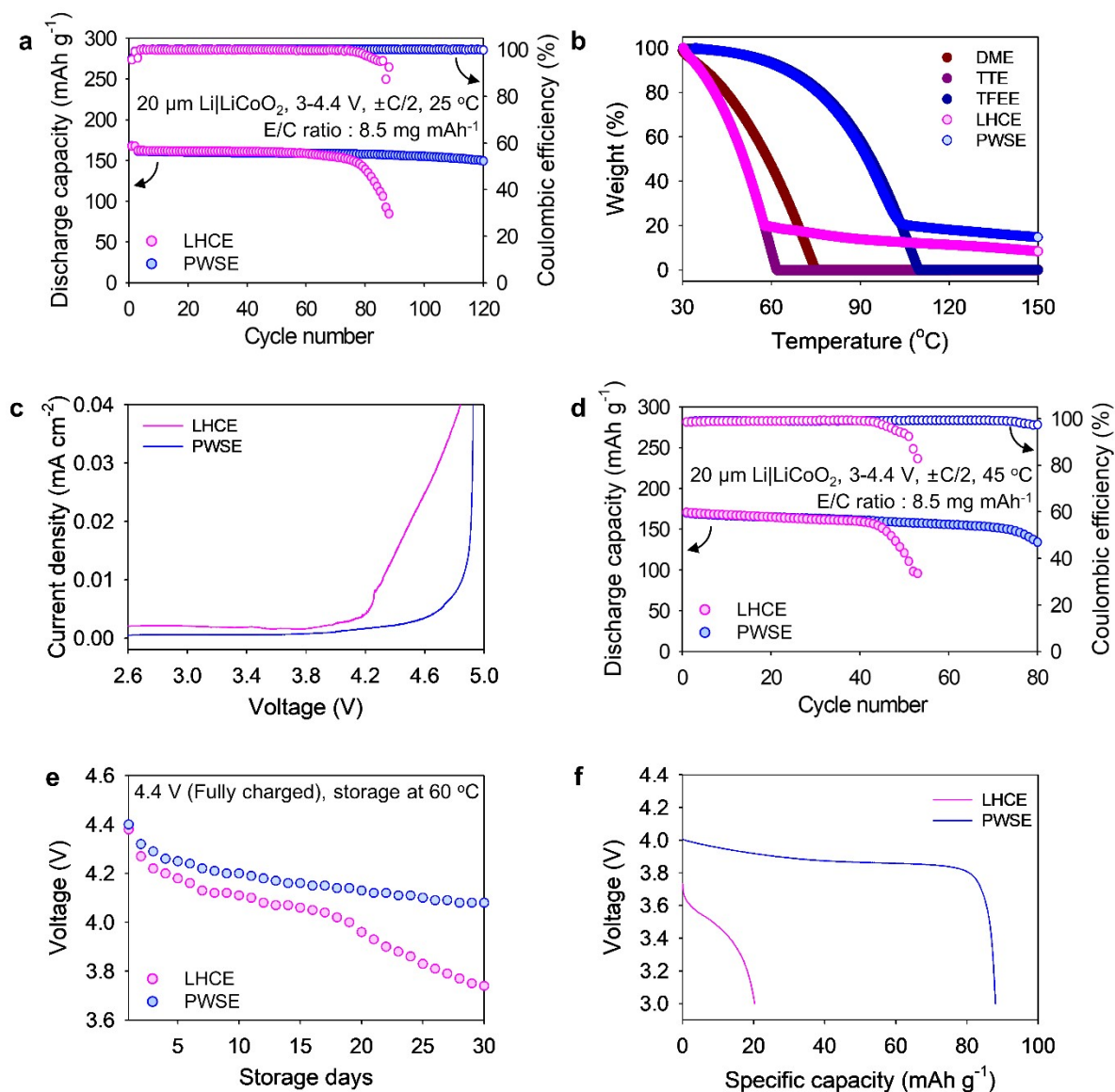


Fig. S76. Comparison of TTE (LHCE) and TFEE (PWSE). (a) Cycle performance of Li|LiCoO₂ full cells with a charge cut-off voltage of 4.4 V vs. Li/Li⁺ at 25 °C. (b) TGA of the solvents (TTE and TFEE) and electrolytes (LHCE and PWSE) from 30 °C to 150 °C. (c) LSV measurements were conducted from the open circuit voltage (OCV) to 5 V vs. Li/Li⁺ at a scan rate of 1 mV s⁻¹ at 45 °C with a stainless-steel working electrode. (d) Cycle performance of Li|LiCoO₂ full cells with a charge cut-off voltage of 4.4 V vs. Li/Li⁺ at 45 °C. (e) Li|LiCoO₂ full cell storage test at 60 °C for 30 days. (f) Capacity retention of Li|LiCoO₂ full cells with the LHCE and PWSE at 25 °C after 30 days of storage at 60 °C.

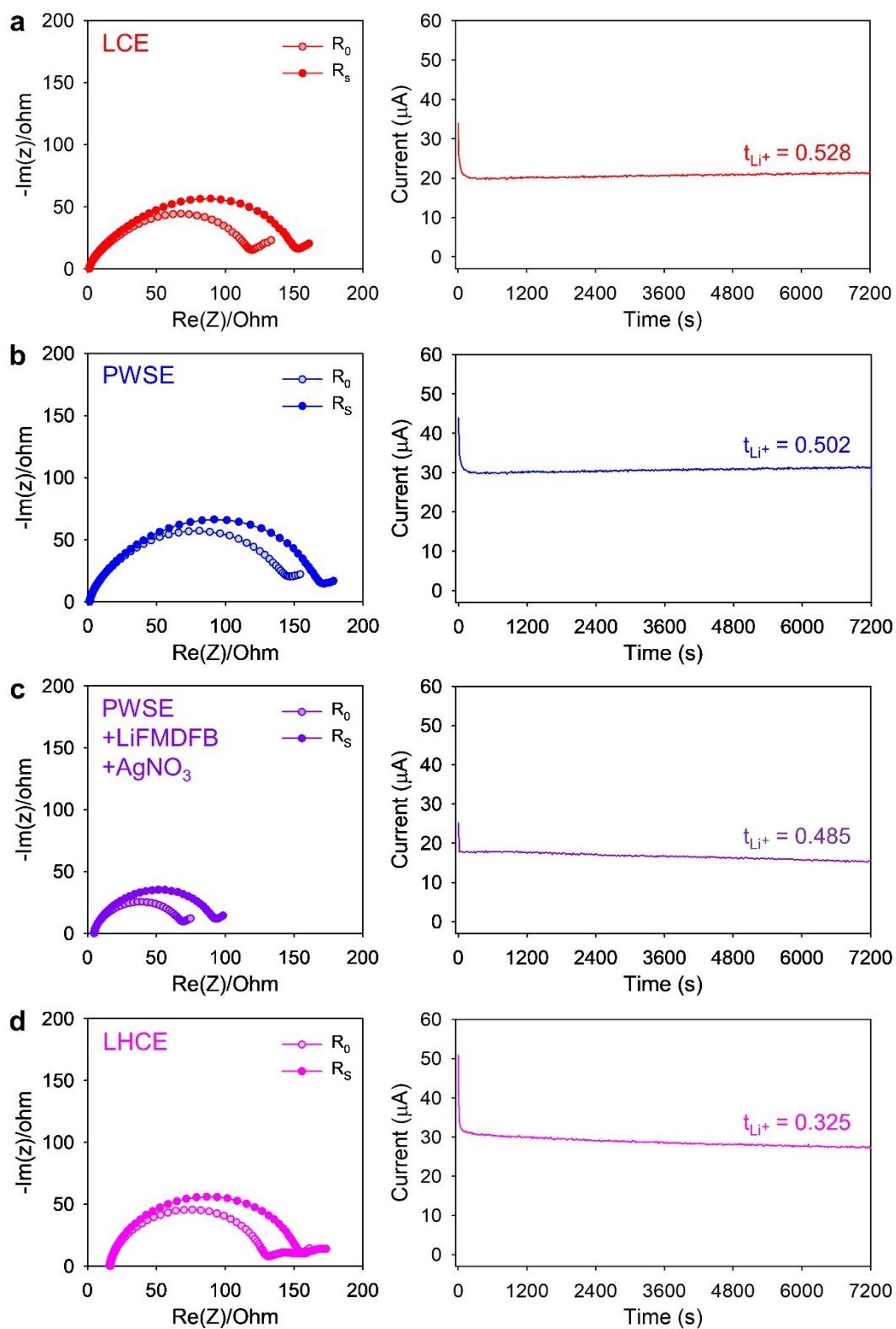


Fig. S77. Li^+ transference number of the electrolytes used in this study (the (a) LCE, (b) PWSE, (c) PWSE+LiFMDFB+AgNO₃, and (d) LHCE).

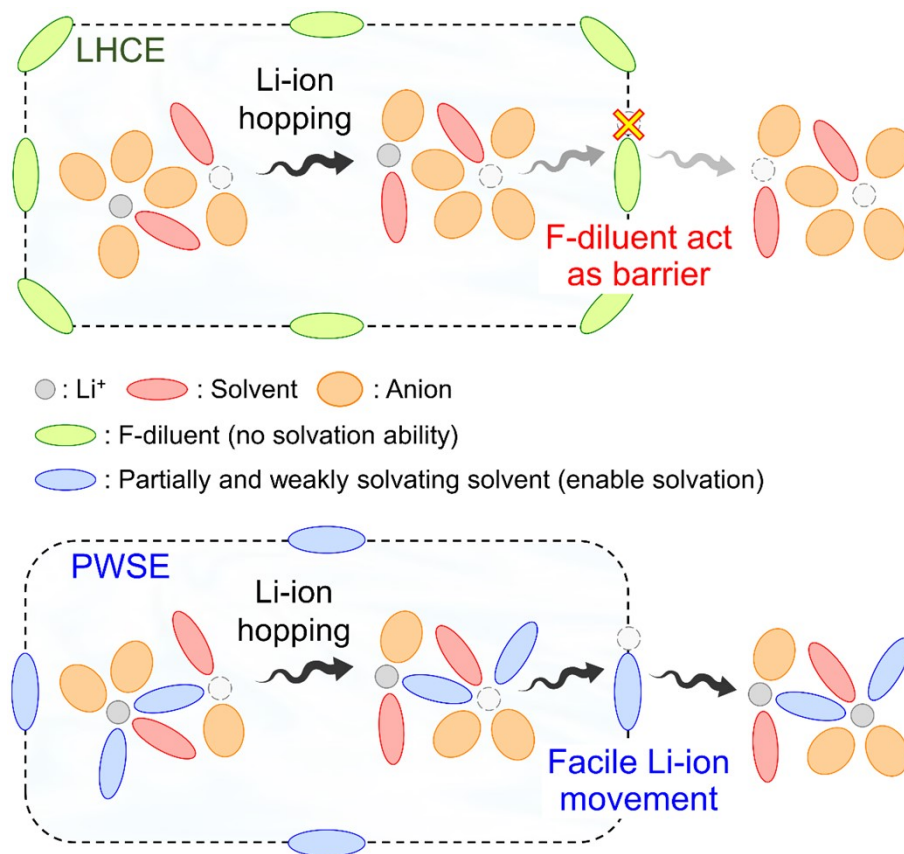


Fig. S78. Schematic illustration of the Li⁺-ion hopping mechanism in LHCE and PWSE.

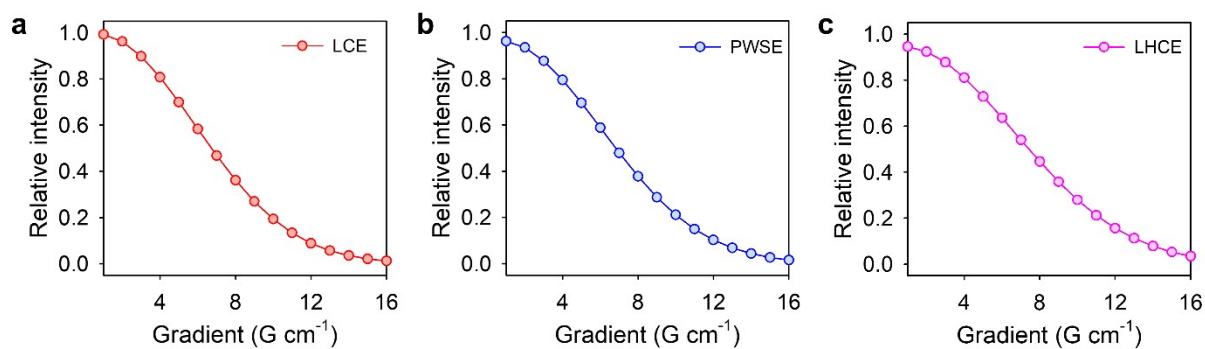


Fig. S79. Intensity decay profiles from the ⁷Li NMR diffusion analysis of the LCE, PWSE, and LHCE.

Supplementary References

1. S. Zugmann, M. Fleishmann, M. Amereller, R. M. Gschwind, H. D. Wiemhofer and H. J. Gores, *Electrochim. Acta*, 2021, **56**, 3926-3933.
2. S. Feng, M. Huang, J. R. Lamb, W. Zhang, R. Tataru, Y. Zhang, Y. G. Zhu, C. F. Perkinson, J. A. Johnson and Y. Shao-Horn, *Chem*, 2019, **5**, 2630-2641.
3. Y. Lee, T. K. Lee, S. Kim, J. Lee, Y. Ahn, K. Kim, H. Ma, G. Park, S.-M. Lee, S. K. Kwak and N.-S. Choi, *Nano Energy*, 2020, **67**, 104309.
4. X.-B. Cheng, R. Zhang, C.-Z. Zhao and Q. Zhang, *Chem. Rev.*, 2017, **117**, 10403-10473.
5. S. Kim, O. S. Park, M.-Y. Lee, J.-A. Lee, I. Kristanto, T. K. Lee, D. Hwang, J. Kim, T.-U. Wi, H.-W. Lee, S. K. Kwak and N.-S. Choi, *Energy Storage Materials*, 2022, **45**, 1-13.
6. C. Fang, B. Lu, G. Pawar, M. Zhang, D. Cheng, S. Chen, M. Ceja, J.-M. Drouot, H. Musrock, M. Cai, B. Liaw and Y. S. Meng, *Nat. Energy*, 2021, **6**, 987-994.
7. M. D. Brennan, M. Breedon, A. S. Best, T. Morishita and M. J. S. Spencer. *Electrochim. Acta*, 2017, **243**, 320-330.
8. Z. Jiang, Z. Zeng, H. Zhang, L. Yang, W. Hu, X. Liang, J. Feng, C. Yu, S. Cheng and J. Xie, *iScience*, 2022, **25**, 103490.
9. Y. Zou, Y. Cheng, J. Lin, Y. Xiao, F. Ren, K. Zhou, M.-S. Wang, D.-Y. Wu, Y. Yang and J. Zheng, *J. Power Sources*, 2022 **532**, 231372.
10. Z. Zhang, F. Liu, Z. Huang, J. Gu, Y. Song, J. Zheng, M. Yi, Q. Mao, M. Bai, X. Fan, B. Hong, Z. Zhang and Y. Lai, *ACS Appl. Energy Mater.*, 2021, **4**, 12954-12964.
11. S. Lin and J. Zhao, *ACS Appl. Mater. Interfaces*, 2020, **12**, 8316-8323.
12. L. Li, G. Xu, S. Zhang, S. Dong, S. Wang, Z. Cui, X. Du, C. Wang, B. Xie, J. Du, X. Zhou and G. Cui, *ACS Energy Lett.*, 2022, **7**, 591-598.
13. S. Lee, K. Park, B. Koo, C. Park, M. Jang, H. Lee and H. Lee, *Adv. Funct. Mater.*, 2020, **30**, 2003132.

14. X. Ren, X. Zhang, Z. Shadike, L. Zou, H. Jia, X. Cao, M. H. Engelhard, B. E. Matthews, C. Wang, B. W. Arey, X.-Q. Yang, J. Liu, J.-G. Zhang and W. Xu, *Adv. Mater.*, 2020, **32**, 2004898.
15. W. Xue, R. Gao, Z. Shi, X. Xiao, W. Zhang, Y. Zhang, Y. G. Zhu, I. Waluyo, Y. Li, M. R. Hill, Z. Zhu, S. Li, O. Kuznetsov, Y. Zhang, W.-K. Lee, A. Hunt, A. Harutyunyan, Y. Shao-Horn, J. A. Johnson and J. Li, *Energy Environ. Sci.*, 2021, **14**, 6030-5040.
16. Z. Jiang, J. Mo, C. Li, H.-W. Li, Q. Zhang, Z. Zeng, J. Xie and Y. Li, *Energy Environ. Sci.*, 2022, **0**, e12440.
17. H. Wang, J. Zhang, H. Zhang, W. Li, M. Chen, Q. Guo, K. C. Lau, L. Zeng, G. Feng, D. Zhai and F. Kang, *Cell Reports Physical Science*, 2022, **3**, 100919.
18. J. Wu, Z. Gao, Y. Wang, X. Yang, Q. Liu, D. Zhou, X. Wang, F. Kang and B. Li, *Nano-Micro Lett.*, 2022, **14**, 147.
19. Y. Zheng, W. Fang, H. Zheng, Y. Su, X. Liang, C. Chen and H. Xiang, *J. Electrochem. Soc.*, 2019, **166**, A3222-A3227.